ARTICLE

Multifunctional Gold Nanoclusters for Effective Targeting, Near-Infrared Fluorescence Imaging, Diagnosis, and Treatment of Cancer Lymphatic Metastasis

Zeyang Pang, Weixiao Yan, Jie Yang, Qizhen Li, Yuan Guo, Dejian Zhou,* and Xingyu Jiang*

Read Online

ACCESS | Metrics & More | Article Recommendations | SI Supporting Information

ABSTRACT: Developing effective lymph-node (LN) targeting and imaging probes is crucial for the early detection and diagnosis of tumor metastasis to improve patient survival. Most current clinical LN imaging probes are based on small organic dyes (e.g., indocyanine green) or radioactive ^{99m}Tc-complexes, which often suffer from limitations, such as rapid photobleaching, poor signal contrast, and potential biosafety issues. Moreover, these probes cannot easily incorporate therapeutic functions to realize beneficial theranostics without affecting their LN-targeting ability. Herein, we have developed dual-ligand-/multiligand-capped gold nanoclusters (GNCs) for specific targeting, near-infrared (NIR) fluorescence imaging, diagnosis, and treatment of LN cancer metastasis in in vivo mouse models. By optimizing the surface ligand coating, we have prepared $Au_{25}(SR_1)_n(SR_2)_{18−n}$ (where SR_1 and SR_2 are different functional thiol ligands)-type GNCs, which display highly effective LN targeting, excellent stability and biocompatibility, and optimal body-retention time. Moreover, they can provide continuous NIR fluorescence imaging of LNs for >3 h from a single dose, making them well-suited for fluorescence-guided surgery. Importantly, we have further incorporated methotrexate, a chemotherapeutic drug, into the GNCs without affecting their LN-targeting ability. Consequently, they can significantly improve the efficiency of methotrexate delivery to target LNs, achieving excellent therapeutic efficacy with up to 4-fold lower hepatotoxicity. Thus, the GNCs are highly effective and safe theranostic nanomedicines against cancer lymphatic metastasis.
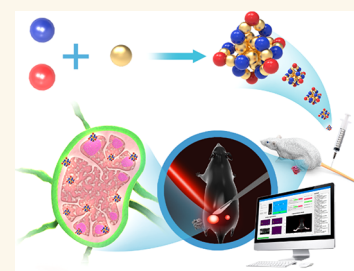
KEYWORDS: gold nanoclusters, cancer metastasis, lymph-node targeting, fluorescence imaging, imaging-guided surgery, theranostics

T umor metastasis is the leading cause of mortality in cancer patients[1,2] and is responsible for ∼90% of cancer-related deaths worldwide.[3,4] Tumor metastasis normally begins from the lymph nodes (LNs) closest to a tumor.[5,6] Cancer cell diffusion through LNs, particularly in highly metastatic melanoma and breast cancer, is critical to cancer metastasis.[7] Thus, lymphatic-based tumor imaging is vital for diagnosing tumor progression[8] and guiding surgical removal of LNs to control the spread of metastasis.[9,10] Current clinical LN metastasis imaging mainly relies on preoperative contrast agents, e.g., ^{99m}Tc-complexes and small organic dyes (isosulfan blue, indocyanine green (ICG), etc.).[11] Unfortunately, these imaging agents often suffer from drawbacks, including biosafety issues, non-real-time imaging, short in vivo half-life, rapid photobleaching, and poor signal contrast. Moreover, the combined use of two or more of such imaging agents does not offer any advantages over their individual use.[12] Furthermore, it is extremely difficult to incorporate therapeutic functions in such imaging agents to convert them into effective theranostic probes without affecting their LN

imaging properties. Thus, there is an urgent need to develop an effective LN-targeting agent that can provide robust, high-resolution, real-time fluorescence imaging of LNs for early diagnosis and imaging-guided surgery of cancer metastasis.[9,13,14] In addition, it would be highly beneficial to integrate imaging and therapeutic functions in one probe to improve theranostics of tumor-LN metastasis.
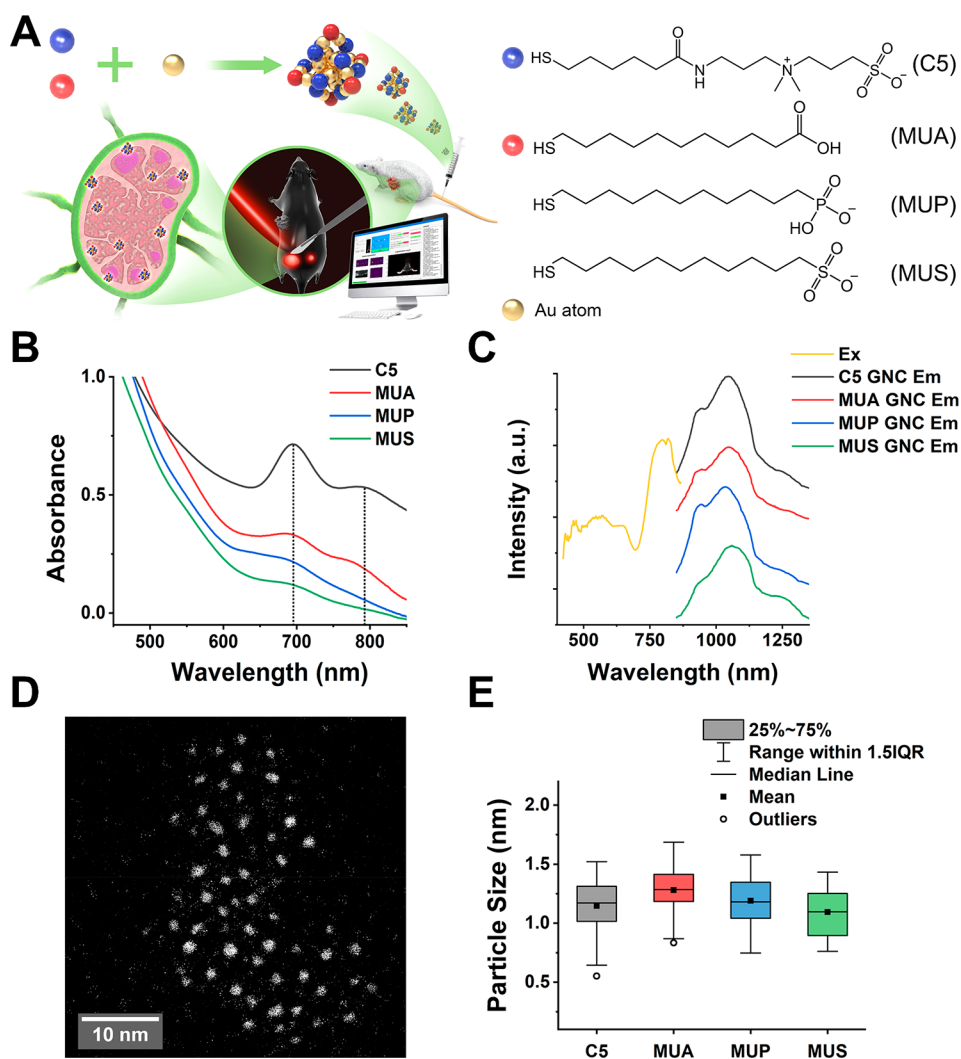
Gold nanomaterials have been widely employed in broad biomedical applications owing to their excellent size tunability, biocompatibility, and versatile gold−thiol chemistry that facilitates surface functionalization.[15−19] Gold nanoclusters (GNCs) containing a few to approximately hundreds of gold
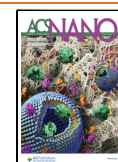
Figure 1. Synthesis and characterization of single-ligand-capped gold nanoclusters (GNCs). (A) Schematic of the study process. Optimal GNCs preferentially accumulate in the lymph nodes (LNs) of mice. Under 808 nm laser irradiation, the NIR-II fluorescence of GNC can provide a high-contrast image to distinguish LNs with and without metastatic foci, thereby guiding LN surgical removal. The right panel shows the chemical structures of the thiolated C5 and anionic ligands used in this study. (B) UV−vis spectra of the GNCs prepared with 100% thiolated zwitterionic ligand (C5), 11-mercaptoundecanoic (MUA), 11-mercaptoundecylphosphonic (MUP), and 11-mercaptoundecylsulfonic (MUS) ligands. All samples show characteristic absorption peaks of the $Au_{25}(SR)_{18}$ GNC (marked with dotted lines). (C) Near-infrared (NIR) fluorescence excitation and emission spectra of the GNCs capped with 100% C5, MUA, MUP, or MUS ligand. The maximum emission peak for all the GNCs is similar and consistent with that of the $Au_{25}(SR)_{18}$-type GNC. (D) Representative figure of 100% C5-capped GNC and (E) box chart of particle sizes for the 100% C5-, MUA-, MUP-, and MUS-capped GNCs, analyzed with a double spherical aberration-corrected transmission electron microscope (DSAC-TEM). The size of the single-ligand-capped GNCs is around 1.2 nm. No notable size differences are observed for the four groups.

atoms have recently emerged as a highly attractive biomedical probe because of their high stability, low toxicity, facile synthesis, and renal clearing ability.[20−23] Moreover, they display robust fluorescence in the second near-infrared region of the biological window (NIR-II, e.g., 1000−1700 nm), making them well suitable for bioimaging because they offer deep tissue penetration, high sensitivity, high-resolution imaging, and minimal autofluorescence background.[24−27] Indeed, NIR-II-fluorescent GNCs have been widely employed for bone imaging,[28] tumor diagnosis,[29,30] angiography,[31] and, more recently, LN imaging.[32] However, recent GNC probes comprise mixed nanoclusters with a varying number of gold atoms, making precise quality control difficult—a highly significant requirement for potential clinical translation and approval. To date, high-purity and atomically precise GNCs

were mostly prepared through the reduction of Au(III) salt in the presence of thiolate ligands, while such GNCs are mostly coated with a single type of thiolated ligand, making it difficult to tailor their surface properties for effective *in vivo* biomedical applications. For example, to access LNs for specific targeting, GNCs must carry some net negative charges because they need to navigate through interstitial spaces filled with intertwined collagen fibers and negatively charged glycosaminoglycan (primarily hyaluronic acid) matrix.[33−35] Thus, the charge density on GNCs is critical as too high or too low surface charge can result in undesirable nonspecific accumulation or rapid renal elimination.[36−38] Thus, preparing GNCs with optimal charge density and excellent stability while minimizing nonspecific interactions with nontarget biomolecules is essential for effective LN targeting. However, those GNCs
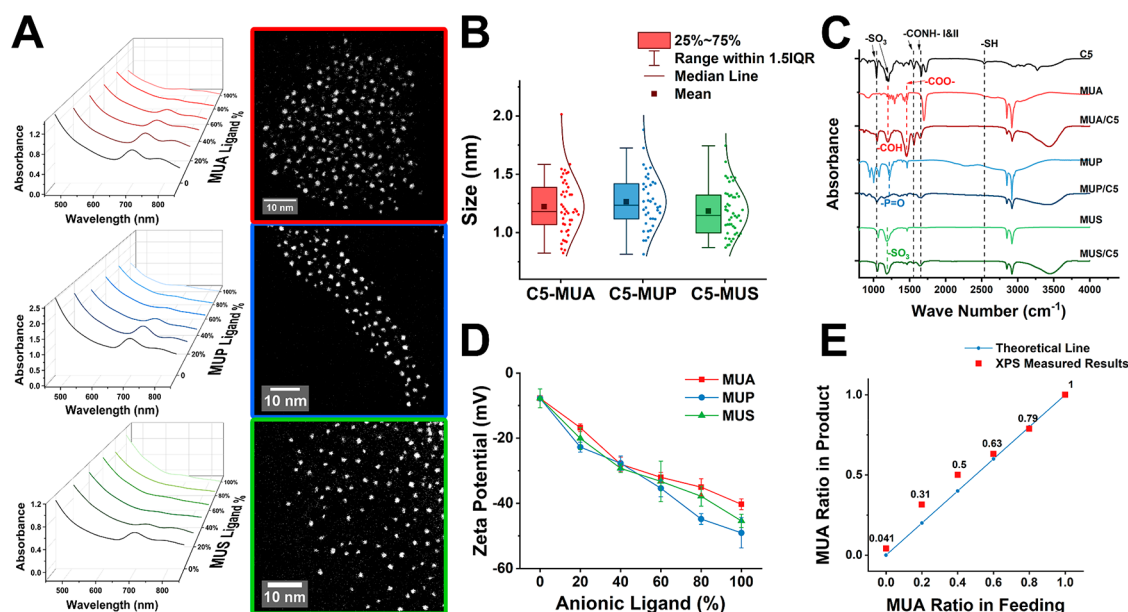
Figure 2. Characterizations of the size distribution and ligand ratio of dual-ligand GNCs. (A) UV−vis spectra (left) and representative DSAC-TEM images (right) of dual-ligand GNCs capped with an increasing ratio of MUA, MUP, or MUS (SR_1) ligand to C5 (SR_2). The absorbance curve gradually becomes smoother with increasing SR_1 ligand proportion. (B) Size statistic box chart of dual-ligand GNCs capped with 50%-50% of C5-MUA, C5-MUP, or C5-MUS ligands. The sizes for the GNCs capped with different ligands are similar, with an average diameter of ∼1.25 nm. (C) Fourier transform infrared (FTIR) spectra of the mono-ligand- and dual-ligand-capped GNCs. The spectra confirm the coexistence of the corresponding negatively charged ligands and C5 on the surface of GNCs. (D) Relationship between the zeta potential and anionic ligand feed percentages of GNCs showing that the GNCs become increasingly more negatively charged with increasing anionic ligand proportion in feeding, confirming the capping of both ligands on the surface of GNCs. (E) XPS data showing the relationship between the yielded percentage of MUA on the dual-ligand GNC and the percentage of MUA in feeding. Compared with C5, the MUA ligand appears to have a higher binding affinity to the Au_{25} kernel over the range of 0−60% in feeding (points above the theoretical line). Further increasing the MUA ligand feeding percentage, the MUA ligand ratio in the product gradually matches that of its feeding ratio.

capped with a single type of thiolated ligand cannot readily meet such requirements. Hence, coating GNCs with two or more types of functional ligands is necessary to impart suitable surface properties for effective LN targeting.

Herein, we report the synthesis of dual-functional/multifunctional ligand-capped and NIR-II-fluorescent $Au_{25}(SR_1)_n(SR_2)_{18-n}$-type GNCs for targeting and effective theranostics of cancer lymphatic metastasis. For specific LN targeting, we have fine-tuned the surface charge group and density of GNCs by varying the feed ratio of anionic to neutral zwitterionic ligands (C5) during the GNC synthesis.[39,40] We have selected three anionic alkylthiol ligands with the same C11 chain length but different terminal acidic groups to control their ionization, e.g., 11-mercaptoundecanoic acid (MUA), 11-mercaptoundecylphosphonic acid (MUP), and 11-mercaptoundecylsulfonic acid (MUS, see Figure 1 for the chemical structures). We found that only the MUA-C5-dual-ligand-capped GNCs can effectively accumulate in LNs and offer high-contrast fluorescence images for sensitive cancer LN-metastatic diagnosis and surgical guidance (Figure 1A). We have further incorporated methotrexate (MTX), a potent cancer chemotherapeutic drug with significant toxicity as a free drug,[41] into the optimal GNC for investigating its potential as a LN-targeted theranostic nanomedicine (Supporting Information (SI), Scheme S3 and Figure S1). The GNC can offer efficient, targeted delivery and excellent therapeutic efficacy against cancer-LN metastasis with dramatically reduced toxicity compared to free MTX in *in vivo* mouse models, thus demonstrating its potential as a highly effective theranostic nanomedicine against cancer lymphatic metastasis.

RESULTS AND DISCUSSION

First, we synthesized GNCs separately with each of the four thiolated ligands (C5, MUA, MUP, or MUS) and recorded their UV−vis spectra. All monoligand-capped GNCs showed prominent characteristic absorption peaks of the $Au_{25}(SR)_{18}$-type GNC at ∼695 and 790 nm (Figure 1B).[42] Electrospray ionization mass spectrometry (ESI-MS) analysis of the GNCs showed clustered MS peaks that matched those expected for the corresponding $Au_{25}(SR)_{18}$-type GNCs (SI, Figure S2 and Table S1).[43] All GNCs exhibited extremely similar fluorescence spectra (Figure 1C)[26] with emissions in the wavelength range of 1000−1100 nm (λ_{EX} = 808 nm)—all within the biological second near-infrared optical transmission window (NIR-II).[29] Double spherical aberration-corrected transmission electron microscope (DSAC-TEM) images collected with a high-angle ring dark-field detector (HADDF)-STEM mode revealed an average diameter of ∼1.2 nm for all GNCs (Figure 1D and E). These results confirm the successful synthesis of the $Au_{25}(SR)_{18}$-type GNCs capped with each of the C5, MUA, MUP, and MUS ligands. Moreover, these GNCs exhibit similar sizes and optical properties. This provides a solid foundation for the subsequent synthesis of atomically precise, dual-ligand-capped GNCs.

We further tuned the feed ratios of MUA-, MUP-, and MUS-to-C5 for preparing various dual-ligand-capped GNCs. All mixed-ligand-capped GNCs showed similar characteristic UV−vis absorption peaks as their monoligand counterparts. In addition, increasing the feed proportion of the negatively charged ligands reduced the intensity of the UV−vis characteristic peak at ∼690 nm (Figure 2A) as well as the

NIR fluorescence brightness of the GNCs (SI, Figure S3). This result is similar to that reported by Aldeek et al.[44] Considering this, the fluorescence intensity of each GNC was normalized and adjusted in subsequent experiments for the direct comparison of the content of GNCs. In addition, the DSAC-TEM images further confirmed a narrow size distribution of ~1.25 nm, comparable to their single-ligand-capped counterparts (Figure 2A and B). Further, ESI-MS tests were conducted to confirm the configurations of the $Au_{25}(SR_1)_n(SR_2)_{18-n}$-type GNCs with different ligand feed proportions. The MS analysis revealed that the MUA exhibited a higher binding affinity to gold kernels than C5, where feeding of 20% MUA yielded $Au_{25}(MUA)_8(C5)_{10}$ as the main product. Further increasing the proportion of MUA in feeding, the ligand composition of the main product gradually matched the ligand feed ratio (Table 1 and SI, Figure S4). Fourier

Table 1. Summary of the Primary and Secondary Formulas of the $Au_{25}(MUA)_n(C5)_{18-n}$ Products Prepared under Different Feed Proportions of MUA Ligand

| MUA ligand proportion (%)	Primary product (n/18−n)	Secondary product(s) (n/18−n)
0	0/18	-
20	8/10	9/9
40	10/8	11/7 and 9/9
60	13/5	12/6 and 14/4
80	16/2	15/3
100	18/0	-

transform infrared (FTIR) spectroscopy analysis confirmed that all ligands were incorporated into the GNCs, as they showed the characteristic IR peaks of the corresponding MUA, MUP, or MUS ligands. The S−H stretching peak at ~2500 cm⁻¹ for free ligands completely disappeared, suggesting that the thiolated ligands were bonded to the GNCs via the Au−S bond, as expected (Figure 2C).[45] The zeta potential of the dual-ligand GNCs became progressively negatively charged with the increasing feed proportion of anionic ligands. This provided a fine control over the negative charge density on the GNC for screening the charge-dependent bioaccumulation (Figure 2D). To illustrate the capping efficiency, X-ray photoelectron spectroscopy (XPS) was also applied to analyze the dependence of the MUA percentage on the surface of produced GNCs as a function of the MUA feed percentage. The N 1s (~402.67 eV) and S $2p_{3/2}$ (~162.70 eV) orbitals were analyzed to measure the abundance of the quaternary ammonium group in C5 and the total Au−S bond. By plotting the MUA percentage in feeding and product, a similar trend to the MS data was observed and reaffirmed a slightly higher affinity for MUA to the Au_{25} kernel than C5. For example, with 20% of MUA in feeding, it accounts for 31% of the total ligands on the GNC surface. However, as the feed percentage of MUA increased to over 60%, this advantage gradually became less obvious, and the MUA percentage in the product gradually matched its feed percentage (Figure 2E). Since the change of ligand feed ratios has an influence on its surface charge, before the subsequent in vivo experiments, we studied the stability of different GNCs in the simulated body fluid environment to rule out differences in their own in vivo stability. Taking MUA-C5 as an example, after incubating dual-ligand GNCs prepared with the MUA feed ratio of 0 to 100% with human serum for 1 week, the fluorescence intensity and

solution properties did not change (Figure S5). The results for MUP-C5 and MUS-C5 GNCs are also the same, which provides a guarantee for our follow-up in vivo experiments.

To study the biodistribution of the GNCs, we intravenously injected them into mice through the tail vein to achieve a rapid whole-body distribution. Next, we anesthetized the mice and used a NIR-II fluorescence animal imager to photograph the supine and prone positions of the mice at different time points for 6 h, taking full advantage of the NIR-II fluorescence of the GNCs for in vivo imaging. We first studied the in vivo distribution of the 100% C5 ligand-capped GNC (Figure 3A). Being a zwitterionic neutral ligand, introducing C5 to the GNC coating can dilute its surface charge density and impart excellent antifouling and antiadsorption properties by forming a strong hydration layer on its sulfobetaine terminal group.[46,47] Therefore, the GNCs capped with 100% C5 should have minimal protein corona formation in vivo, yielding a hydrodynamic size well below the renal clearance threshold (~6.4 nm);[48,49] hence, rapid renal clearance with short body retention was expected. Indeed, strong NIR-II fluorescence was observed in the bladder shortly after intravenous injection (I.V.), whereas the fluorescence signals in other body parts faded quickly, indicating a rapid renal clearance of the GNCs as expected.

Subsequently, the biodistribution of the GNCs capped with mixed C5-MUA ligands was studied. As shown in Figure 3A, increasing the MUA proportion from 0 to 20% could slightly increase the GNC body retention and renal clearance time (to ~2 h), accompanied by higher liver and kidney accumulations, although its overall in vivo biodistribution still resembled that of the pure C5-capped GNC. As the MUA proportion was increased to 40%—60%, noticeable fluorescence signals were found in the LNs at 2 h post-I.V., as indicated by an intense and lasting signal in the sacral part of the prone position, suggesting high lymphatic accumulation. Further increasing the MUA proportion to >60% led to the disappearance of lymphatic accumulation, where the GNCs were mainly retained in the liver and spleen, as indicated by prominent fluorescence. Moreover, urine samples collected hourly post-I.V. further supported the GNC renal clearance results observed in NIR-II fluorescence imaging (SI, Figure S6). The hydrodynamic size of GNCs in vivo was strongly affected by protein corona formation, which was closely related to the negative charge density of GNCs.[36] Thus, the ability of GNCs with 40%−60% MUA to accumulate in LNs was attributed to the anionic charge-induced size changes in vivo, as confirmed by the zeta potential result.

To illustrate how the surface negative charge density of the GNCs may affect their size in vivo, we performed a gel electrophoresis study of the GNCs prepared with different MUA proportions with and without human serum. Figure S7 (SI) shows that with increasing MUA proportion, the gap between the electrophoresis bands of the GNCs with and without human serum became wide. Particularly, in the presence of human serum, the tailing effects became more obvious. This result indicates that the MUA ligand leads to the observed nonspecific interactions between GNCs and serum proteins due to electrostatic interactions. The strength of the interactions increased with increasing MUA proportion, leading to extensive protein corona formation on the GNCs that increases their overall size. Previously, organ distribution tropism of lipid nanoparticles (NPs) was achieved by tuning the overall surface charge.[50] In addition, the size of lipid NPs
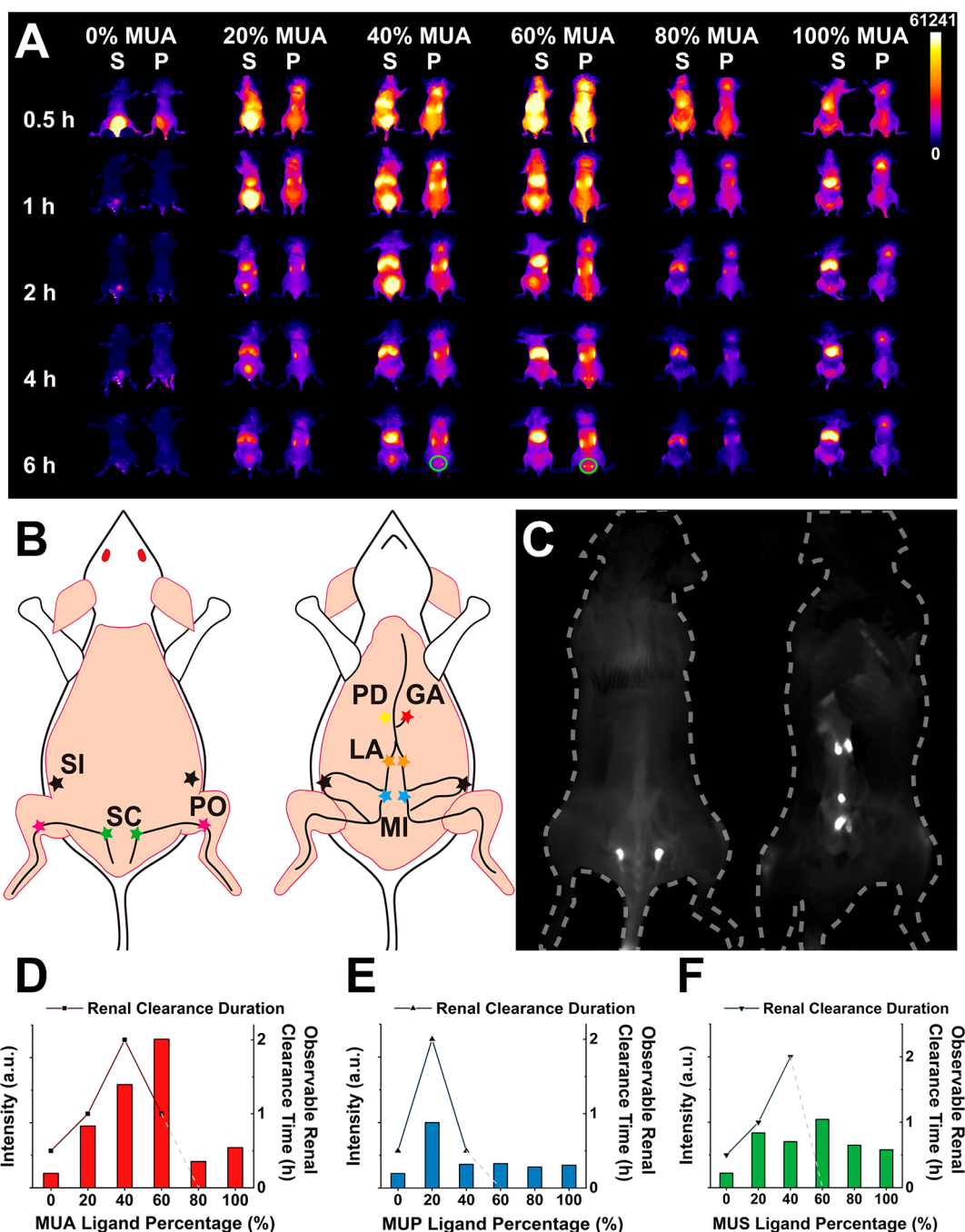
Figure 3. *In vivo* distribution of dual-ligand-capped GNCs with different proportions of anionic ligands. (A) Time- and MUA feed percentage-dependent NIR-II fluorescence images showing the *in vivo* distribution of GNCs in mice after the intravenous injection (I.V.) of GNC (5 mg kg^{-1}) for 6 h (S, supine position; P, prone position; the same as below). Dual-ligand GNCs with 40%−60% MUA in feeding are effectively accumulated in the LNs located in the sciatic area (labeled with green ovals, 30 ms, 20 mW cm^{-2}). (B) Distribution map of some LNs in the middle and lower body of mice. Different pairs of LNs are marked with different colors. GA, gastric LN; LA, lumbar aortic LN; MI, medial iliac LN; PD, pancreatic oduodenal LN; PO, popliteal LN; SC, sciatic LN; and SI, sub iliac LN. (C) NIR-II fluorescence image showing the accumulation of the GNCs within the lower-body LNs of mice under 808 nm laser excitation. Six hours after I.V., the GNCs with 50% MUA in feeding are effectively accumulated in the LNs near the spine. Even for gastric LNs that are far away from the injection site, the GNCs can provide a strong fluorescence contrast for guiding surgical resection (left, prone position; right, supine position; 20 ms, 20 mW cm^{-2}). (D−F) Plots of the GNC fluorescence intensity in sciatic LNs and renal clearance time against the anionic ligand feed proportions of (D) MUA, (E) MUP, and (F) MUS.

was found to strongly affect their biodistribution, with smaller NPs (∼30 nm) offering higher LN accumulation.[51] Further, the size of the GNCs was found to be a critical factor in determining their renal clearance due to excess glomerular barriers.[52] These literature reports can explain the reduced renal clearance and increased LN accumulation observed herein. Because the size of the GNC−protein corona complexes increased with increasing anionic charges, the *in vivo* clearance of the GNCs shifted from the urinary to the hepatic pathway, accompanied by reduced distribution within
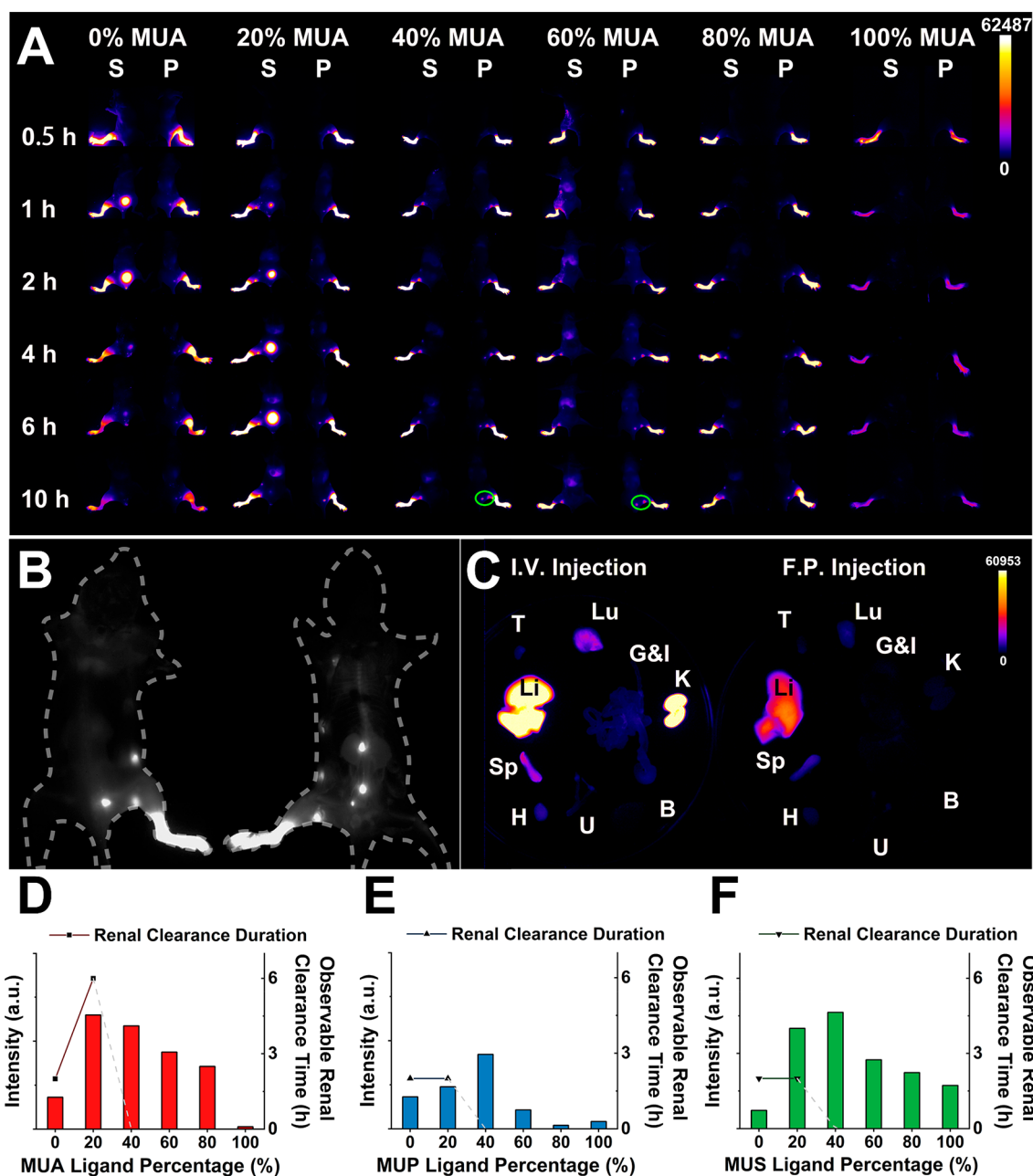
Figure 4. *In vivo* distribution of the dual-ligand GNCs with different anionic ligand proportions administered through a right footpad injection (F.P.). (A) NIR-II fluorescence images showing the distribution of GNCs with different MUA proportions after F.P. over 10 h. GNCs prepared with ≤20% MUA proportion demonstrated renal clearance times of up to 6 h, whereas those prepared with 40%−60% MUA feeds displayed a high retention rate in popliteal and sciatic LNs (labeled with green ovals; S, supine position; P, prone position; the same as below; 25 ms, 20 mW cm^{-2}). (B) NIR-II fluorescence image showing the *in vivo* distribution of the GNCs prepared with 50% MUA proportion under 808 nm laser irradiation at 10 h after F.P.; GNCs accumulated in unilateral lower-body LNs, including popliteal and sciatic LNs. Some LNs stained during I.V. were also visible in the F.P. result (left, prone position; right, supine position; 20 ms, 20 mW cm^{-2}). (C) NIR-II fluorescence images of major organs harvested from mice 10 h post-administration of GNCs with 50% MUA proportion *via* different administration methods (B, brain; G&I, gastrointestinal tract; H, heart; K, kidneys; Li, liver; Lu, lungs; Sp, spleen; T, thymus; U, uterus; 20 ms, 20 mW cm^{-2}). Plots of the relationship between fluorescence intensity in popliteal LNs and renal clearance time against the anionic ligand feed proportion for (D) MUA, (E) MUP, and (F) MUS ligands.

LNs.[53] Thus, the optimal balance of the clearance and LN distribution can be achieved by tuning the feed proportion of the anionic and zwitterionic ligands during GNC preparation.

The lower body and hind limbs of the mouse have abundant lymphatics and LNs, including popliteal, sciatic, inguinal, lumbar, gastric, and iliac LNs (Figure 3B).[54−57] We conducted anatomy studies and found that the fluorescence signals appeared not only in LNs close to the injection site, such as sciatic LNs (first-draining), but also in remote sites, such as gastric LNs (Figure 3C). The quantum yield (QY) of the GNC prepared with 50% MUA proportion was 1.48%, higher than most water-soluble NIR-II fluorescent GNCs and comparable to some small molecular NIR fluorescent dyes.[28,30,58] Combining the advantageous properties of high QY and
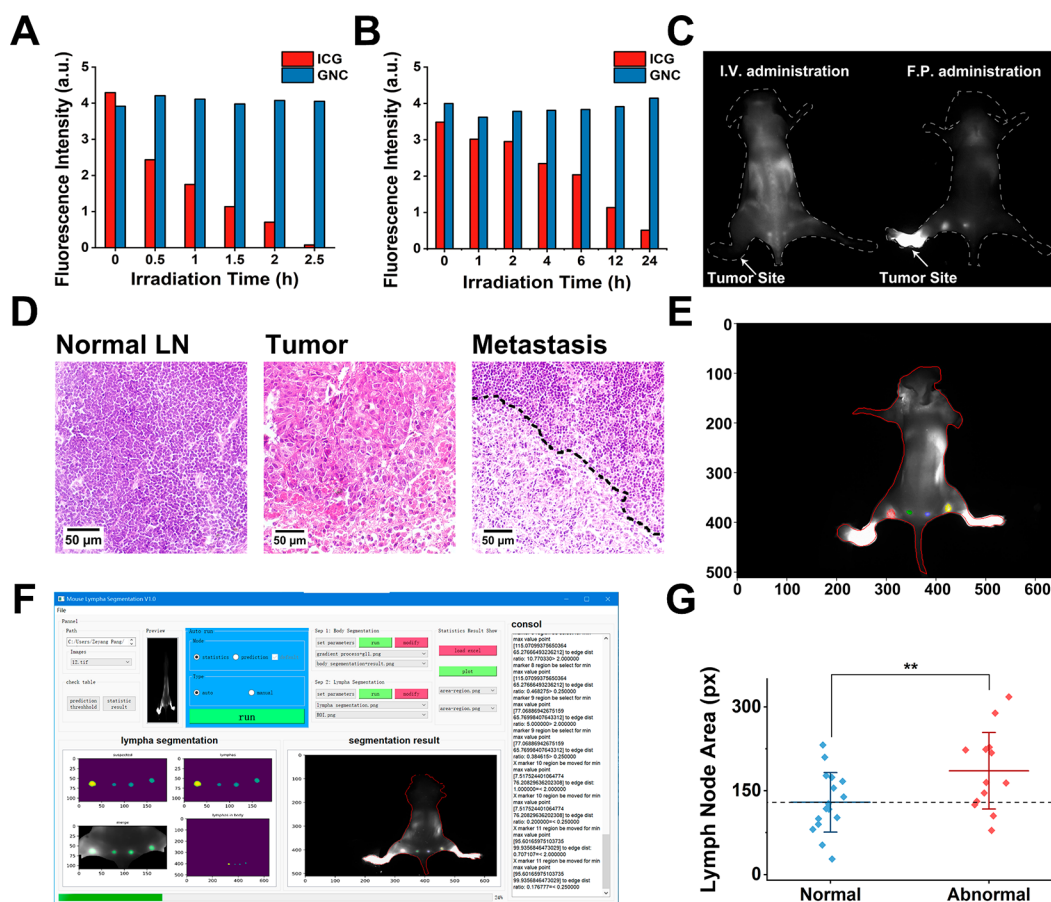
Figure 5. Comparison of the photostabilities of the MUA-GNC and indocyanine green (ICG) and application of the MUA-GNC for imaging in an *in vivo* mouse footpad tumor model. Relative intensity bar charts of GNC and ICG on exposure to (A) direct laser irradiation (808 nm, 20 mW cm^{-2}) and (B) indoor light irradiation. The fluorescence of ICG was rapidly photobleached by an 808 nm laser with a short half-life of ~0.5 h, whereas the fluorescence of GNC remained unaffected. (C) NIR-II fluorescence images showing the use of the MUA-GNC in the direct imaging of LN metastasis with *in situ* tumor models administered through I.V. (left) and F.P. (right). Both methods could detect the abnormal size of metastatic LNs, although F.P. showed a higher fluorescence contrast in LNs next to the injection site and lower background away from the injection site (tumor marked with white arrows, 20 ms, 20 mW cm^{-2}). (D) Hematoxylin and eosin (H&E) staining of the LN section revealed tumor metastasis in the first-draining LNs, confirming the ability of the MUA-GNC to detect LN metastasis. The dotted line indicates the boundary between the normal LN and tumor tissues. (E) Recognition process of body outline and lower-body LNs with the help of the home-developed image-analysis program. (F) Screenshot showing the automatic drawing of the mouse outline and the recognition of LNs in the user interface of the program. (G) Box chart showing the distribution of the LN fluorescence areas between the tumor-bearing and normal legs. There is a statistical difference between the two groups of data. The threshold was set to be 130 pixels (**, $0.01 < P < 0.05$).

excellent LN-targeting ability, this GNC offered a high signal-to-background ratio of approximately 60 in the LN region. Such high-contrast fluorescence images are extremely beneficial for noninvasive diagnosis and imaging-guided surgeries of LNs. Unexpectedly, the dual-ligand GNCs prepared with varying proportions of the MUP or MUS ligands showed an insignificant accumulation in LNs, as evidenced by substantially lower fluorescence signals in LNs than those for the MUA-capped GNCs (SI, Figure S8). This result indicates that the LN-accumulation property of the GNCs is dependent on the density and the type of negatively charged groups decorated on their surface.

We plotted the renal clearance duration and LN fluorescence intensity 6 h after I.V. against the ligand feed proportion (Figure 3D−F). A clear trade-off was observed between the GNC lymphatic accumulation and renal clearance time, which could be controlled by the anionic ligand type and feed proportion.[17,59] This result implies that tuning the surface negative charge density of the GNCs is an effective way of

developing lymphatic targeting probes. In this regard, a weakly ionizable ligand (e.g., MUA, terminal CO_2H pK_a = ~4.95) is more suitable than the strongly ionized ones, e.g., MUS (pK_a = ~ −1) or MUP (pK_a = ~ 2.1).[60] Notably, the pK_a values of the GNC bond ligands are expected to be higher than those of the corresponding free ligands.

To study how the administration methods affect the LN-targeting properties of GNCs, we further compared the footpad injection (F.P.) outcome with the I.V. data. F.P. is a common technique for lymphatic dosing because the hind limb region of mice has abundant lymphatics and LNs.[61] Generally, lymphatic accumulation away from blood circulation is poor because the epithelial cell gap of lymphatic vessel capillaries is substantially higher than that of blood vessels.[33] Besides, the blood flow rate is approximately 100−500 times that of lymphatic flows, which can hinder the GNC transportation within lymphatics.[62] However, F.P. could directly drain GNCs to lymphatics through the interstitium to increase their contact with the lymphatic system. Thus, F.P. can increase the LN-

accumulation efficiency of GNCs while reducing accumulation in other organs.[37] Due to the relatively slow process of crossing the interstitial space, we extended the observation time to 10 h. As shown in Figure 4A, the entirely zwitterionic-ligand-capped GNCs exhibited a relatively fast renal clearance time of ~2 h. As the MUA ligand feed increased to 60%, popliteal and sciatic LNs in the injection site showed intensive fluorescence and were easily distinguished from the surrounding tissues. Consistent with the I.V. results above, the LN-targeting ability of the MUA-capped GNCs was better than that of the GNCs capped with MUP or MUS ligand (Figure 4A and SI, Figure S9). Through these studies, we concluded that the GNCs prepared with 40%−60% MUA proportions can provide effective LN targeting. Thus, we used 50% MUA as the optimal ligand feed for the GNC preparation in all further experiments (denoted as MUA-GNC hereafter). The MUA-GNC administered through F.P. was restrained in LNs close to the injection site, including popliteal (first-draining), sciatic, subiliac, and medial iliac LNs (Figure 4B). Moreover, pathology analysis confirmed that F.P. resulted in less overall GNC accumulation in the main organs than I.V., particularly in the liver and kidneys, potentially reducing the toxic side effects caused by nondesirable hepatic and renal accumulation (Figure 4C). For all three anionic ligand-capped GNCs, the relationship between the LN accumulation and ligand feeds for the F.P. and I.V. was similar. Moreover, the relationship between the GNC-surface negative charge density and renal clearance time, as shown above, was also similar for MUP- and MUS-capped GNCs (Figure 4D—F).

To find the relationship between the GNC concentration in the lower-body LNs and the exposure time of the NIR imager, we injected an equal volume of serially diluted GNC solutions into the mouse footpad and optimized the exposure time to give similar fluorescence intensities (SI, Figure S10A). Using the MUA-GNC at doses as low as 1.2 mg kg^{-1}, we could still acquire a low-latency video with high contrast. However, because the common frame rate of videos is 30 frames per second, the delay time should be ≤33 ms to avoid inconsistencies between the video and operation. Thus, a dose of 5 mg kg^{-1} of the MUA-GNC was deemed optimal for recording real-time videos. It could provide a short exposure time of 17 ms and avoid waste of materials.

As one of the most common NIR bioimaging fluorophores, ICG has been widely used for lymphatic imaging and fluorescence-guided surgery.[63] Unfortunately, ICG-based *in vivo* imaging suffers from several apparent limitations, including high hemoglobin affinity, short plasma half-life (2−4 min), low hydrophilicity, and difficulty in chemical modification.[64,65] Moreover, it suffers from rapid photobleaching, limiting its effective imaging time to 30 min,[66] which is insufficient for deep LN-related surgeries that often last for several hours.[58] Besides, its narrow absorption and small Stokes shift require a matching laser source for excitation and optical filters for imaging.[67,68] Thus, developing capable probes for sensitive, long-lasting NIR fluorescence imaging is urgently needed. We first compared the photostability of the MUA-GNC and ICG under an 808 nm laser irradiation (20 mW cm^{-2}) (Figure 5A and SI, Figure S10B). The fluorescence of ICG rapidly decreased upon exposure to irradiation, losing ~50% of the initial intensity within 30 min and becoming almost completely photobleached at 2.5 h, indicating poor photostability. In contrast, the MUA-GNC showed no observable changes in fluorescence during the entire 2.5-h

laser radiation period, demonstrating highly robust photoluminescence. We also compared their fluorescence stabilities upon exposure to a household incandescent lamp (15 W, ~1125 lm) (Figure 5B and SI, Figure S10C). Similarly, the ICG fluorescence decreased continuously and retained just ~10% of the initial intensity at 24 h, indicating poor photostability and aqueous stability.[69] However, the fluorescence of the MUA-GNC remained almost constant throughout the 24-h exposure, reaffirming its excellent photostability and aqueous stability. Thus, the use of GNCs for bioimaging would not require strict light-shielding, making it more convenient for *in vivo* imaging. Furthermore, the MUA-GNC was excited efficiently using a white light from an LED lamp (12 W, ~1200 lm) to emit strong NIR fluorescence, whereas ICG was completely nonfluorescent under such conditions (SI, Figure S10D). This is another significant feature of MUA-GNC-based bioimaging, which can be efficiently excited by various exciting light sources without affecting the emission. In addition, the MUA-GNC effectively retained its NIR fluorescence after lyophilization, which is convenient for storage and transportation and is important for practical applications (SI, Figure S10E).

We constructed an *in situ* lymphatic metastasis model by injecting Hep3B human hepatocarcinoma cells into the footpad of mice. After I.V. and F.P. of the MUA-GNC, we could distinguish between metastatic and normal LNs from the NIR-II fluorescence images, where metastatic LNs showed a significantly increased volume and irregular shapes (Figure 5C). Moreover, we conducted an imaging-guided surgery to remove sentinel LNs (Supporting Video), where the stained LNs showed bright NIR-II fluorescence and strong contrast from surrounding tissues, making surgical resection convenient. Even though not professionally trained in surgery, the operator could easily judge the location of LNs as well as their status and perform a resection operation to remove the metastatic LN entirely. After an operation, LN samples were stained with hematoxylin and eosin (H&E) to confirm the existence of the metastatic region mixed with normal tissues (Figure 5D). We further constructed heterotopic tumor models, including intraperitoneal and subcutaneous models, to demonstrate the potential of the MUA-GNC in imaging-guided surgeries. In the heterotopic models, F.P. of the MUA-GNC yielded high NIR-II fluorescence contrast, allowing for feasible diagnosis and surgically removing LNs (SI, Figure S11). These results demonstrate the successful use of the MUA-GNCs for the noninvasive diagnosis of tumor-LN metastasis and NIR-II fluorescence-guided surgery.

To further demonstrate the potential of the MUA-GNC for the diagnosis of tumor-LN metastasis, a self-developed recognition program was designed and tested. We established an *in situ* tumor model on the unilateral footpad of mice. Then, the GNCs were administrated through bilateral F.P., and after 6 h, the NIR fluorescence was photographed to compare the size and fluorescence intensity of bilateral sentinel LNs (PO LNs). The LNs in the left and right legs of a single mouse were used as self-control. By inputting the NIR images, our program could automatically recognize the body outline of mice and distinguish the LN position (Figure 5E and F). The GNC-aided identification of the size differences between the experimental and control groups showed statistical differences. The accuracy of recognition was >65.5% (Figure 5G). These results confirm the potential of the MUA-GNC to act as an
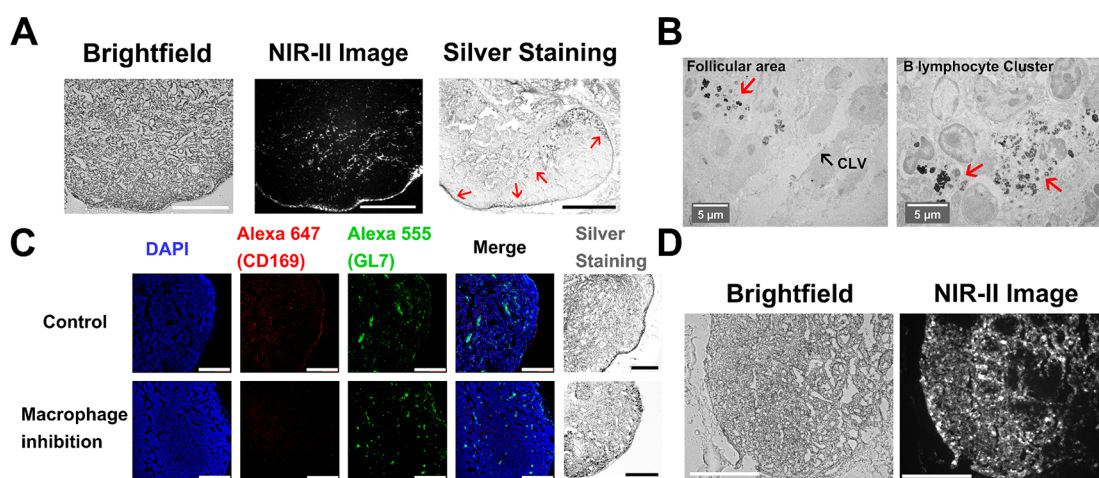
Figure 6. Investigation of the effect of subcapsular sinus (SCS) macrophage depletion on the distribution of MUA-GNC in LNs through tissue sections. (A) Bright-field, NIR-II fluorescence and silver-stained optical images of LN harvested from mice after treatment with MUA-GNC for 10 h. GNC was mainly distributed in the cortex region around the capsular region of LNs. It could also enter the deeper cortex and distribute in the lymphatic follicles (labeled with red arrows; scale bar: 200 μm). (B) TEM images of the MUA-GNC-treated LN tissue after silver staining to show its distribution in LNs. The silver staining signals are marked with red arrows. A GNC signal was found in follicles and the B cell cluster region, indicating its ability to pass through cortical lymphatic vessels and reach the follicular area (CLV, cortical lymphatic vessel; scale bar: 5 μm). (C) Confocal images showing the effect of macrophage suppression on the GNC distribution within the LNs. The macrophage-inhibited group showed significantly reduced SCS macrophages with the enhanced infiltration of MUA-GNCs compared to the control group (Alexa 647, CD169-SCS macrophages; Alexa 555, GL7-Geminal center; scale bar: 200 μm). (D) Bright-field and NIR-II fluorescence images of the LN section showing that GNC was no longer restricted to the subcapsular lymphatic sinuses and penetrated deeply into the paracortex layer for the macrophage-inhibited group (scale bar: 200 μm).

effective surgical guidance and LN metastasis diagnostic reagent.

To examine the penetration depth of the MUA-GNC in LNs, we prepared 20-μm-thick frozen sections of LNs (6 h after F.P.) and monitored the GNC fluorescence on a NIR microfluorescence imaging system. Compared with the bright-field image, the fluorescence signal appeared either near the afferent lymphatics and lymphatic sinuses or in a deeper cortex region. To locate the MUA-GNC position within the LN, we prepared 5-μm-thick LN sections and applied silver staining to amplify the GNC signals for easy confirmation. Consistent with the NIR fluorescence image, the optical image of silver-amplified GNCs was found to accumulate mainly near the afferent lymphatics, subcapsular sinus, and follicular area (Figure 6A, marked by red arrows). The corresponding LN TEM images further revealed that GNCs had penetrated the lymphatic sinus into the follicles and interacted with B lymphocytes (Figure 6B).[70] These results suggest that the MUA-GNCs are widely distributed within LNs and have extensive contact with several LN-residue immune cells.

Besides the dispersed macrophages in lymphatics and antigen-presenting cells in follicles, the subcapsular sinus (SCS) macrophages in LNs also play an important role in antigen capture and presentation, although their role in nanomaterial distribution remains unclear.[71] Previous studies have shown that SCS macrophages obstruct nanoparticles from entering LN follicles by capturing and endocytosing them.[70] To probe the role of SCS macrophages in the MUA-GNC distribution in LNs, we treated mice with GdCl$_3$ (a macrophage inhibitor) 3 days before GNC application and compared the GNC distribution with that of the phosphate buffer saline (PBS) control.[72] We prepared 5-μm-thick LN sections and stained the germinal center (B lymphocyte clusters) and SCS macrophages with anti-GL7 (green) and anti-CD169 (red) antibodies, respectively, and the GNC

deposition was monitored by silver staining (Figure 6C). Comparing the SCS macrophage and GNC locations in the control group, we found extensive colocalization of both in subcapsular regions, indicating that SCS macrophage plays an important role in the retention of GNCs within LNs.[73]

Macrophage suppression was confirmed by the disappearance of red fluorescence in the SCS area, accompanied by a higher germinal center formation, possibly resulting from higher retention of MUA-GNCs within the follicles without SCS macrophage obstruction. The silver staining result also revealed a different GNC distribution pattern compared to that of the control, where the former exhibited substantially lower retention in the subcapsular area and deeper distribution in the cortex and paracortex layers than the latter. Additionally, the GNC NIR-II fluorescence was also different from that of the control, showing reduced surface interception and deepened distribution. This result agreed well with that of the silver staining, indicating that SCS macrophages hinder GNC LN distribution and accumulation (Figure 6D). Together, these results revealed that removing SCS macrophages at the entrance to the follicles led to higher overall accumulation and deeper penetration of GNCs in LNs, as confirmed by a stronger MUA-GNC fluorescence. The function of SCS macrophages in GNC accumulation discovered herein can provide useful guidance for the design of LN-targeting nanomaterials.

The elimination process is a vital indicator for the biosafety of bioimaging agents.[74] The MUA-GNC pharmacokinetic profile in the blood and main organs in mice was analyzed by measuring the Au content. The plasma half-life ($T_{1/2\alpha}$, distribution half-life) of the MUA-GNC was measured to be ~0.83 h, which is significantly higher than the plasma half-life of ICG (e.g., 3−4 min), meaning that there is sufficient time for the MUA-GNC to accumulate within the peripheral LNs before clearance (SI, Figure S12). In addition, the Au contents
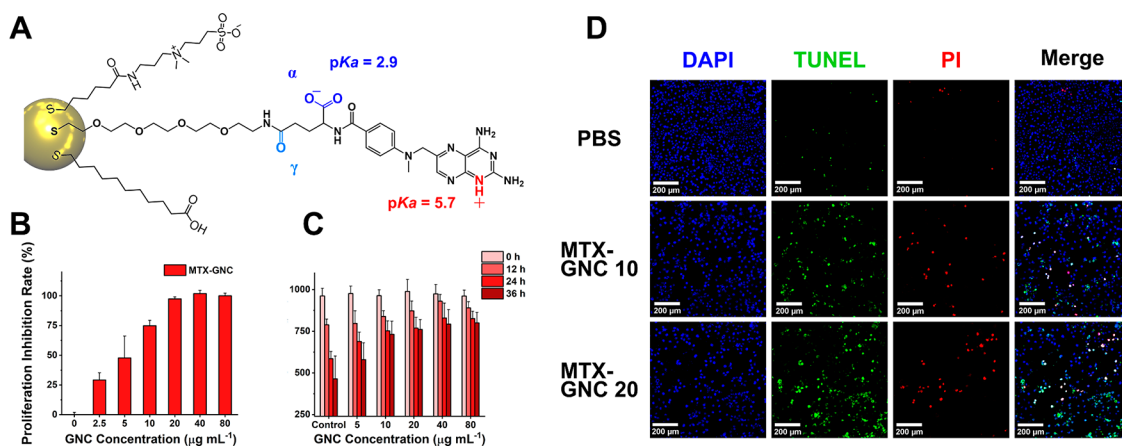
Figure 7. Structure of MTX-loaded triligand GNC and characterization of its antitumor effect *in vitro*. (A) Schematic diagram of triligand MTX-GNC. The MTX molecule was covalently linked to an amino PEG chain through formation of a highly stable amide bond, and all three ligands are attached to GNC through the Au−S bond. Under normal physiological pH (7.35−7.45), the α-carboxylic acid (pK_a = ∼2.9) of the HS-MTX ligand will be fully deprotonated, while the N in the pteridine ring (pK_a = ∼5.7) will be nonprotonated to give an overall one net negative charge. (B) *In vitro* antiproliferation effect of MTX-capped GNC on the HUH-7 cell line, wherein ∼100% inhibition of tumor cell growth was achieved at ∼20 μg mL^{-1}. (C) Summary of the scratch-healing results for treatments with different MTX-capped GNC concentrations. (D) Cell staining results showing the apoptosis rate of HUH-7 cells after a 24 h treatment of PBS and 10 or 20 μg mL^{-1} MTX-GNC. The apoptosis rate was analyzed by staining with terminal deoxynucleotidyl transferase-mediated dUTP-biotin nick end labeling (TUNEL) and propidium iodide (PI), which can be used to detect early and late apoptosis, respectively.

in the main organs in mice, including the heart, lungs, liver, kidneys, and spleen, were also measured (SI, Figure S13). Consistent with the renal clearance results (SI, Figure S6), the Au content in the kidney decreased rapidly within the first 4 h and then gradually leveled off. In contrast, the Au content in the liver, spleen, and lungs showed a gradual increase from 2 h to the end of the experiment (12 h). A gradual increase of the Au content in the reticuloendothelial system (RES) organs after the reduction of renal clearance indicated that the RES organs were the main clearance pathways for the remaining GNCs. We further extended the observation time to investigate the thorough clearance time of the MUA-GNC. Due to a small size and moderately negative surface charge, the body-retention time of the MUA-GNC was found adequate for *in vivo* imaging: its fluorescence signal in the liver and LNs decayed gradually and became almost invisible 96 h after I.V. administration (SI, Figure S14A). Thus, a single injection of the MUA-GNC can satisfy the requirement of imaging-guided surgery, avoiding the need for repeated injections of ICG for the same purpose due to its short *in vivo* half-life.[63] For F.P., the retention within the injection site was approximately 144 h. To verify the biosafety of the MUA-GNC, we conducted an *in vitro* live−dead staining of human umbilical vein endothelial cells using Calcein-AM and propidium iodide after a 24-h treatment with PBS (control) or 100 or 200 μg mL^{-1} GNC (SI, Figure S14B). There was no obvious difference in the number of dead cells for the control and MUA-GNC-treated groups. Further, an *in vivo* safety test was conducted by injecting 40 mg kg^{-1} GNC (eight times the dosage used in the imaging above) into the tail vein or footpad, and biochemical indices, including blood routine and liver and kidney function indexes, were measured 3 days after injection. Even at such a high dosage, pathological examination of organs confirmed no apparent histopathological changes (SI, Figure S14C). The biochemical indices of both GNC groups showed no significant differences from those of the control group, and all of these were within the normal range (SI, Figure S15). Together, these results demonstrate that the MUA-GNC has

high biosafety and can be safely used in various bioimaging applications.

We further explored the application of MUA-GNCs in treating cancer metastasis, taking advantage of their potent LN-accumulation capacity. Here we incorporated methotrexate (MTX), a classic cancer chemotherapeutic drug inhibiting DNA synthesis and cell proliferation, into the MUA-GNC.[75] Despite being highly effective in treating multiple cancer types, MTX exhibits undesirable whole-body distribution, resulting in high hepatotoxicity and nephrotoxicity.[41] Moreover, the requirement for frequent dosing of MTX due to a short half-life can further worsen its side effects.[76] Based on the good LN-targeting ability of the MUA-GNC, we hypothesized that it could serve as an effective nanocarrier for the targeted delivery of MTX into LNs to reduce drug toxicity. Because each MTX molecule contains two carboxylic acid groups (α- and γ-), it can be conveniently coupled to a thiolated tetra(ethylene glycol) amine through the formation of an amide linkage to yield thiolated methotrexate (HS-MTX) (Figure 7A).[77,78] After coupling, there are two ionizable groups in the HS-MTX ligand: the free α-CO$_2$H (pK_a = ∼2.9) and the quaternized 2,4-diaminopteridyl (pK_a = ∼5.7) group. Under the physiological pH of 7.4 used in our study, the free α-CO$_2$H group will be fully deprotonated to CO$_2^-$ while the quaternary ammonium group should be mostly nonprotonated (∼98%) and, hence, be mostly neutral. Thus, under our experimental conditions, each HS-MTX molecule should carry one net negative charge, the same as the MUA ligand.[79] We further adjusted the ligand feed ratio to HS-MTX:MUA:C5 = 3:5:5 (proportion of total negatively charged ligand: ∼60%) and prepared the triligand-capped GNC (abbreviated as MTX-GNC hereafter). The loading efficiency of MTX on the MTX-GNC was estimated from the MTX amount difference between that added and that remaining unbonded after MTX-GNC preparation against a standard MTX-concentration calibration curve, giving an HS-MTX loading efficiency of 70.5 ± 0.7% in a single-batch MTX-GNC synthesis.[80] The MTX-GNC showed the characteristic UV−vis absorption
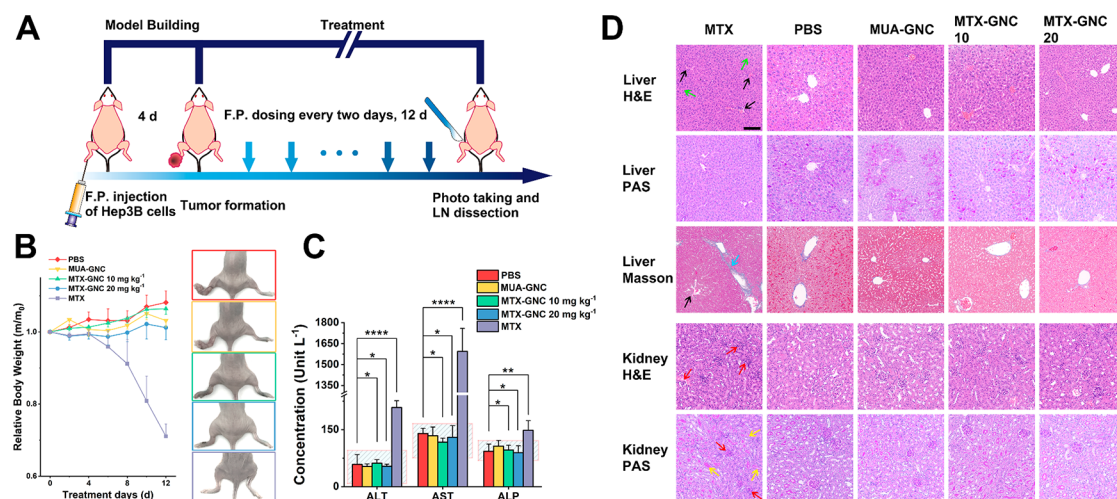
Figure 8. Comparison of free MTX and MTX-GNC treatments showing that the MTX toxicity was significantly reduced after capping it onto MUA-GNC. (A) Experimental flow chart of tumor modeling and treatment. (B) Left: change in the bodyweight of tumor-bearing mice following different treatment processes. Right: pictures of the tumor-bearing body part (left footpad) and skin appearance. Free-MTX-treated mice were in an unusually emaciated state with significantly decreased bodyweight, whereas all other groups showed no significant weight loss or changes in appearance ($n = 5$). (C) Comparison of liver biochemical indices for mice after different treatments. Only the free MTX treatment group showed abnormally high alanine aminotransferase (ALT), aspartate aminotransferase (AST), and alkaline phosphatase (ALP) levels, indicating acute liver damage, whereas these indicators in all other groups were comparable and within the normal range ($n = 4$; ****, $P < 0.001$; **, $0.01 < P < 0.05$; *, $P > 0.05$). (D) H&E, periodic acid-Schiff (PAS), and Masson staining of liver and kidney tissues after different treatments: black arrows, degeneration of liver sinusoids and cords; green arrows, hepatocyte necrosis; azure arrow, hepatic fiber bridging; red arrows, glomerular damage and fibrosis; yellow arrows, brush borders shedding.

peaks of the MTX-free counterparts (SI, Figure S16A). Its size was also similar to that of the MUA-GNC (SI, Figure S16B and C). Treatment of the MTX-GNC dose-dependently reduced the viability of HUH-7 cells, a liver cancer cell line, with an IC_{50} of ~5.4 μg mL^{-1}, demonstrating a good anticancer potency (Figure 7B).

An in vitro scratch-healing test was further conducted to visualize the inhibitory effect of the MTX-GNC on the proliferation and migration of HUH-7 cells. Cells treated with ≥5 μg mL^{-1} of the MTX-GNC yielded extremely low cell proliferation efficiency compared to the negative control, confirming that HS-MTX maintained its antiproliferation properties after loading onto the GNC (Figure 7C and SI, Figure S17). Free MTX has the strong ability to induce cell apoptosis.[81,82] We thus measured if the MTX-GNC retained the apoptosis-inducing ability of free MTX. HUH-7 cells were incubated with 10 and 20 μg mL^{-1} MTX-GNCs for 24 h, and terminal deoxynucleotidyl transferase-mediated dUTP-biotin nick end labeling (TUNEL) and propidium iodide (PI) staining were applied to distinguish early and late apoptosis (Figure 7D). Compared with the low TUNEL (1.12%, green-to-blue ratio) and PI (0.56%, red-to-blue ratio, same below) signals for the PBS control, the TUNEL and PI signals of the 10 μg mL^{-1} MTX-GNC group were significantly increased to 14.2% and 5.66%, respectively, while those for the 20 μg mL^{-1} group were further increased to 39.3% and 10.7%, respectively, indicating that the MTX-GNC retained an excellent ability to induce apoptosis in a dose-dependent manner. In addition, under 808 nm laser irradiation, bright NIR fluorescence was captured in the cytoplasm of HUH-7 cells with a NIR fluorescence microscopy imaging system after MTX-GNC treatment (SI, Figure S18), confirming that the MTX-GNC has successfully delivered MTX into cancer cells to induce cell apoptosis.

Having good stability under normal physiological environments is crucial for the MTX-GNC to act as a useful in vivo imaging reagent. As the MTX molecule is bonded to the GNC surface by forming a strong Au–S bond via a covalently linked tetra(ethylene glycol) thiol linker, we expect it to be highly stable. Consistent with our expectation, the MTX content released from the MTX-GNC (measured via a competitive enzyme-linked immunosorbent assay test kit) was found to be negligible (<0.068%) even after a 48-h incubation in 25% human serum, confirming a good in vivo stability. Moreover, the fluorescence of the MTX-GNC in simulated body fluids (PBS + various human serum contents) also showed no observable changes after extended storage of 7 days (SI, Figure S19A). Furthermore, no change in physical appearance or precipitation was observed after 7 days of storage in human serum (SI, Figure S19B). These results confirmed the good stability of the MTX-GNC in the body fluids. We further studied the stability of the MTX-GNC under environments with different pH, while apparent agglutination was observed in strongly acidic environments (e.g., pH ≤ 3); likely due to the protonation of carboxyl groups that weakened electrostatic repulsion of GNCs, their NIR-fluorescence was retained (SI, Figure S19C). However, no aggregation or change of fluorescence was observed for the MTX-GNC across the normal physiological pH range (e.g., pH = 5−8) even after 7 days, indicating that the MTX-GNC has high stability under the in vivo environment.

We then injected the MTX-GNC via F.P. (5 mg kg^{-1}, the same dose as the MUA-GNC above) into mice and found that its fluorescence intensity and in vivo distributions were similar to those of the MUA-GNC, indicating that the co-capping of the HS-MTX has negligible effects on the biophysical properties of the MUA-GNC (SI, Figure S20A).

We further extended the anticancer studies to in vivo lymphatic metastasis models. A LN-metastatic mouse model
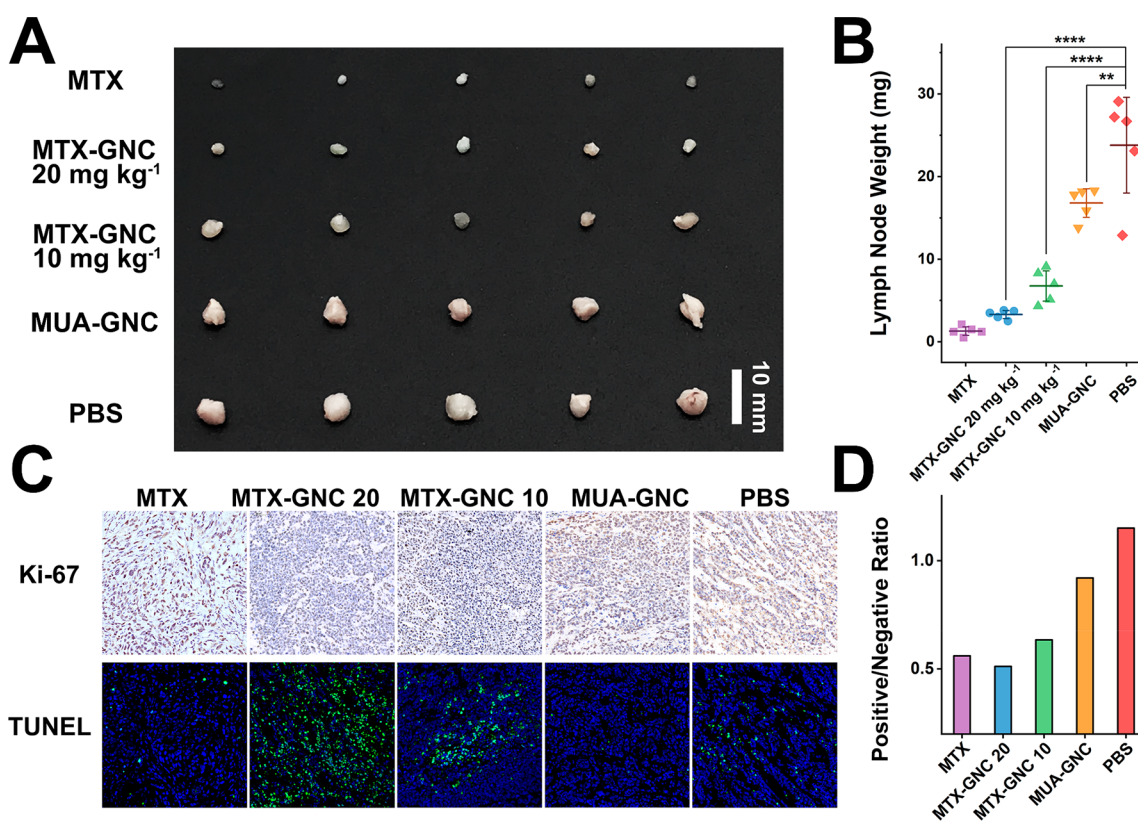
Figure 9. Anti-metastasis properties of MTX-GNC, free MTX, and other treatments. (A) Optical images of ipsilateral popliteal LN harvested from mice after treatments. The size of LNs was reduced after the MTX-GNC treatment in a dose-dependent manner. (B) LN mass statistics of different treatment groups. ($n = 5$; ****, $P < 0.001$; **, $0.01 < P < 0.05$). (C) K_i-67 and TUNEL staining showing the proliferation of tumor tissue and the degree of cell apoptosis. The significantly lower brown color and high green fluorescence in the 20 mg kg^{-1} of MTX-GNC indicate a successful control of tumor cell growth. (D) K_i-67 staining statistical result of the brown (positive) to blue (negative) ratio.

was constructed by injecting human hepatocarcinoma cell-Hep3B cells into the left hind limb footpad of mice. Four days after the injection, the ipsilateral popliteal LN swelled. We then treated the different groups through F.P. of free MTX (5 mg kg^{-1}, equivalent to 15 mg kg^{-1} the MTX-GNC in drug dosage, positive control), the MTX-GNC (10 or 20 mg kg^{-1}), the MUA-GNC (20 mg kg^{-1}), or PBS (negative control), once every 2 days for 12 days. The mice were then sacrificed and photographed, and their LNs were measured (Figure 8A). Only the free MTX treatment group showed a sharp decrease (~30%) in body weight, while all other groups were normal (Figure 8B). Moreover, the free-MTX-treated mice were extremely skinny and weak with rough and dull skin, suggesting severe drug-induced injuries by side effects. These results are consistent with the systemic toxicity of the administration of free MTX. In contrast, treatment with a high dosage of the MTX-GNC resulted in minimal changes in body weight throughout the treatment, indicating its minimal side effects. We also measured the liver and kidney function indices of different groups. For the free MTX group, the alanine aminotransferase (ALT), aspartate aminotransferase (AST), and alkaline phosphatase (ALP) levels were ~4-, ~10-, and ~1.5-fold higher than their expected normal ranges, whereas such indices for all other groups were all within the normal ranges (Figure 8C and SI, Figure S20B). Notably, a substantially enlarged AST/ALT ratio indicates severe liver damage and hepatic fibrosis processes.[83] Here, the AST/ALT ratio was ~8 for the free MTX group, whereas that for both the PBS control group and the MTX-GNC-treated group was

~1.9–2.4. Thus, the MTX-GNC can significantly reduce the hepatotoxicity of free MTX by up to 4-fold. Moreover, the H&E-stained liver slices revealed that, except for the free MTX group, all liver cells were arranged radially centered on the central vein, and the liver lobules were orderly structured (Figure 8D). The hepatic cords were neatly arranged, and the liver lobules were intact without apparent pathological changes. In contrast, in the free MTX group, most of the hepatocytes in the liver lobules were swollen, and the sinusoids and hepatic cords disappeared (black arrows). In addition, the cytoplasm texture was disordered, and local liver cells appeared in necrosis (green arrows).[84] Periodic acid-Schiff (PAS) staining of the glycogen content revealed moderate rose-red coarse particles (PAS staining positive) in the cytoplasm and nucleus of hepatocytes in the PBS control group,[85] and the glycogen content was abundant and evenly distributed. In the GNC treatment groups, glycogens were found to be abundant and mainly distributed in the proximal part of the central vein. In sharp contrast, the liver glycogen almost disappeared in the free MTX group. This negative PAS stain indicated a greatly reduced enzyme activity and glycogen synthesis in the liver. Moreover, the fibrosis process of liver cells could also accelerate the consumption of glycogen. Under such chronic conditions, the glycogen content in the liver cells was gradually depleted. To characterize the degree of fibrosis in the liver, we stained liver sections using the Masson staining method to stain collagen fibers blue. In the free MTX group, severe fibrosis and extensive fiber bridging between portal areas and structural disorders in the liver lobules were observed (azure

arrow), indicating chronic hepatitis fibrosis. However, these were not observed in all other groups. For kidneys, the H&E staining results of all other groups showed a normal renal tissue structure with complete nephrons and no pathological changes in the glomerular or renal interstitium.[86] However, for the free MTX group, obvious pathology occurred at glomerular atrophy (red arrows). There were significant increases in the mesangial matrix, proliferation of the mesangial cells, thickening of the basement membrane, and accumulation of red staining material in the lumen.[87] Moreover, PAS results further revealed a structural disorder, brush border loss, and accumulation of disintegrated cell debris in the lumen (yellow arrows).[88] Together, these results demonstrated that the MTX-GNC had retained the therapeutic effect of free MTX but significantly reduced its toxic side effects *in vivo*.

Due to the fusion of tumor tissue with the footpad, it is difficult to separate and compare the tumor size in each group. Alternatively, we measured the cross-sectional size of the tumor-bearing footpad in each group (SI, Figure S20C), and the corresponding pictures are shown in Figure 8B (insets). The MTX-GNC-treated groups showed great tumor volume regression compared to the PBS and MUA-GNC control groups. We dissected the ipsilateral popliteal LNs next to the injection site and compared their masses and volumes, which indicate the extent of metastasis for all treatment groups (Figure 9A and B,and SI, Figure S20D). The PBS and MUA-GNC control groups showed significantly swollen LNs, indicating serious lymphatic enlargement due to the cancer cell proliferation and immune response.[89] In contrast, treatment with MTX-GNC yielded a substantial, dose-dependent reduction of the LN size and weight compared to the controls. The LN size and weight for the 20 mg kg^{-1} MTX-GNC group were reduced to ~1/7 and 1/5 of that of the PBS control and MUA-GNC-treated groups, respectively. In addition, the average LN size in the 20 mg kg^{-1} MTX-GNC group was only 1.6 times that of the free MTX group, indicating a comparable inhibitory effect on lymphatic metastasis to free MTX. Taking into consideration that the liver and kidney toxicity of free MTX was greatly reduced by using MTX-GNC-based targeted LN delivery (as demonstrated in Figure 8B—D and SI, Figure S20B), the use of the MTX-GNC for *in vivo* treatment not only can alleviate the hepatorenal toxicity issues of free MTX but also can achieve a good antimetastasis effect.

We further applied K_i-67 and TUNEL staining to the tumor-bearing tissue and compared the cell carcinogenesis (by analyzing the K_i-67 content) and apoptosis rate (by analyzing the broken DNA with TUNEL stain) among all the groups (Figure 9C and D). Due to high anticancer potency, the free MTX treatment greatly suppressed cancer cell loading, resulting in almost no observable apoptotic cells. Importantly, the MTX-GNC treatment also showed excellent control of cancer cell growth with significant apoptosis of tumor cells. Our results have demonstrated that the MTX-GNC not only can effectively inhibit lymphatic metastasis and tumor growth but also can greatly reduce the side effects and toxicity of free MTX toward the liver and kidney. Therefore, the MTX-GNC is a safe, highly effective theranostic nanomedicine for targeting, imaging, diagnosis, and treatment of cancer LN metastasis *in vivo*. Together, our results confirm that capping HS-MTX onto the MUA-GNC to form a triligand-GNC-based LN delivery system can greatly reduce the systemic toxicity of the free drug while effectively retaining its anticancer efficiency,

making it a potent approach for developing effective nanomedicines for targeted lymphatic drug delivery and theranostics of LN-related diseases.

CONCLUSIONS

In summary, we have successfully prepared lymphophilic NIR-II fluorescent GNCs based on the atomically precise $Au_{25}(SR_1)_n(SR_2)_{18-n}$-type GNCs that are capped with mixed zwitterionic and anionic ligands. By optimizing the anionic ligand type and feed proportion, our optimal GNC exhibits highly efficient LN accumulation. Moreover, it also displays bright NIR-II fluorescence and is far more stable and user-friendly than ICG—a widely used commercial LN imaging agent, making it well-suited for LN-metastatic diagnosis and surgical guidance. The GNCs show good penetration into the lymphatic follicular area that can be further enhanced *via* SCS macrophage depletion. Furthermore, we have successfully loaded a hepatotoxic chemotherapeutic drug (MTX) onto the GNC for effective tumor metastasis treatment without onerous chemical synthesis. Our MTX-loaded GNC not only can provide excellent antitumor efficacy comparable to free MTX but also can significantly reduce the liver toxicity of the free drug. Combining advantageous features such as excellent photostability, biosafety, ease of synthesis, and high therapeutic potency, our multifunctional GNC can effectively replace current commercial bioimaging agents in a wide range of biomedical research, e.g., targeting, diagnosis, imaging-guided surgery, and treatment of tumor-LN metastasis, with great potential for clinical translation.

MATERIALS AND METHODS

Materials. Reagents mentioned below were purchased from Sigma-Aldrich, except for the following: AcS-PEG$_4$-NH$_2$·HCl (Tansh-Tech, China); NaOH (Aladdin, China); mercaptoundecyl-sulfonic acid (MUS) (Prochimia Surfaces, Poland); anhydrous ethanol (Aladdin, China); ultrathin copper mesh (EMCN, China); 2.5% glutaraldehyde solution (Leagene Biotechnology); phosphate buffer saline (Gibco, USA); AURION R-Gent SE-EM silver staining kit and AURION R-Gent SE-LM silver staining kit (Aurion, Netherlands); 4% paraformaldehyde solution (Alfa Aesar, USA); Tissue-Tek O.C.T. Compound 4583 (SAKURA, USA); adhesive glass slide (JIANCHENG Bioengineering Institute, China); Tris-HCl buffer pH = 7.4 (BIO-RAD, USA); 10% goat serum solution (Boster Bio, USA); citric acid antigen retrieval buffer pH = 6.0 (Servicebio, China); 3-(4,5-dimethyl-2-thiazolyl)-2,5-diphenyltetrazolium bromide (MTT) (InvitrogenTM, USA); anticoagulant test tubes and procoagulant test tubes (HARVEYBIO, China); gadolinium chloride (Alfa Aesar, USA). Sources of antibodies and test kits are illustrated in the corresponding methods.

Synthesis of Thiolated Methotrexate (HS-MTX). HS-MTX was synthesized in two steps. Step 1: MTX was covalently coupled to an actylthiol-PEG$_4$-linker to form acetylthiol-PEG$_4$-modified MTX (SI, Scheme S1). Briefly, to a solution of dimethylformamide (2 mL) containing methotrexate (MTX) (94.5 mg, 0.21 mmol), 2-(1H-benzotriazol-1-yl)-1,1,3,3-tetramethyluronium hexafluorophosphate (HBTU) (75.8 mg, 0.20 mmol) and AcS-PEG$_4$-NH$_2$·HCl (33.1 mg, 0.11 mmol) was added, followed by N,N′-diisopropylethylamine (66 µL, 0.4 mmol), and the resulting mixture was then stirred at 25 °C for 12 h. After that, the reaction mixture was purified by semipreparative high-performance liquid chromatography (HPLC, LC-20AR, SHI-MADZU) to give the target compound, acetylthiol-MTX, as a light-yellow powder in 43.7% yield (35.2 mg).

Step 2: Base deacetylation to give the final HS-MTX (SI, Scheme S2). Briefly, acetylthiol-MTX obtained in the previous step (35.2 mg, 0.048 mmol) was dissolved in 2 mL of water containing 4.0 mg of NaOH (0.10 mmol) and was then stirred at 25 °C for 12 h. After that,

the reaction mixture was purified using semipreparative HPLC to yield the target compound, HS-MTX, in 60.7% yield (20.1 mg).

Synthesis and Characterization of GNCs Capped with Different Ratios of Anionic Ligands. The $Au_{25}(SR)_{18}$-type GNC capped with a single type of ligand was synthesized by following our established procedures.[20] Briefly, an aqueous solution of chloroauric acid tetrahydrate (20 mM, 250 μL) was mixed with the target ligand (5 mM, 2 mL in H_2O). The mixed solution quickly turned golden yellow, indicating the formation of the Au(I)-SR intermediate complex. After that, a varying volume of 1 M NaOH aqueous solution (e.g., 80, 50, 50, and 15 μL for C5, MUA, MUP, and MUS, respectively) was added to the above reaction mixture and then followed by ethanol addition to give a final volume% of 20% for C5, MUA, and MUS and 10% for MUP. Here, a mixed ethanol/water solvent system was used to increase the solubility of the ligand and GNC to avoid precipitation. After that, $NaBH_4$ dissolved in a 0.2 M NaOH aqueous solution (50 μL, 100 mM) was added dropwise to the above reaction mixture under continuous and vigorous stirring. After stirring for 3 h, the GNC product was purified by using Amicon Ultrafiltration Units (MW 3 kDa cutoff) and washed with deionized water until the pH of the filtrate was neutral.

The dual-ligand GNCs were synthesized under identical conditions, except where the ligand used above was replaced by a mixture of two target ligands (e.g., C5 mixed with MUA, MUP, or MUS) in predefined feed ratios, while the total ligand-to-Au ratio was always kept the same as above. Moreover, the amount of NaOH and ethanol added to the reaction was also adjusted according to the weighted average of each ligand.

For MTX-GNC synthesis, the MUA/C5 dual-ligand system was replaced by a HS-MTX-MUA-C5 triligand system at a ligand molar ratio of 3:5:5 while keeping the total ligand concentration and volume the same. All other conditions were the same as that used in the preparation of the MUA/C5 dual-ligand GNC (SI, Scheme S3).

FTIR Sample Preparation. The GNC solution was lyophilized to a loose brown powder and dried using an infrared dryer to remove the water content. 1−2 mg of the GNC was ground with KBr into a fine powder, transferred to a mold, and pressed into flakes with a hydraulic oil press under 5×10^7 Pa. A Thermo Scientific Nicolet iS5 infrared spectrometer was used to measure the FTIR absorption spectroscopy.

Zeta Potential Analysis. The zeta potential of GNCs was measured using a Zetasizer Nano ZS 90 (Malvern Panalytical) equipped with a DTS1070 disposable folded capillary cell. The samples were properly diluted to a light-brown solution (final concentration around 200 μg mL^{-1}) and loaded directly into the equipment.

UV−Vis Spectrophotometer and Near-Infrared Fluorescence Spectrum Test. The GNC solution was properly diluted (final concentration of ∼250 μg mL^{-1}) before being tested via a UV−vis spectrophotometer (UV-2600i, SHIMADZU), steady-state/transient fluorescence/phosphorescence spectrometer (FLS980, Edinburgh Instruments), or near-infrared fluorescence spectrometer (iHR320 equipped with an InGaAs detector, HORIBA). *Origin 2018* was used to process the data.

ESI-MS Characterization of the GNC. The ESI-MS analysis was performed by diluting the freshly prepared GNC stock solution with water 3−5-folds to achieve a final concentration of ∼200 μg mL^{-1}. The samples were injected directly into the atomization system without mobile phase dilution (Q Exactive Plus Hybrid Quadrupole-Orbitrap Mass Spectrometer, Thermofisher). The raw data were further deconvoluted with Thermofisher Protein Deconvolution Software with MH+ mode. The resolution at 400 m/z was set to 50000, and the S/N threshold was set to 3, with the Min Num Detected Charge set to 2.

XPS Characterization of the GNC. For XPS analysis, the GNCs with different ligand feed ratios were prepared following the previous methods and lyophilized as brownish powders. The powder was then placed on a foil with conductive tape attached, pressed into a flake by a tableting machine, cropped to fit, and pasted on a clean sample stage. The samples were then analyzed with an X-ray photoelectron spectrometer (K-Alpha+, Thermo Fisher Scientific) with a mono-chromatic Al Kα X-ray source. The applied energy is 1486.6 eV, 6 mA × 12 kV (72 W) with beam spot size 30−400 μm. The scan mode is constant analyzer energy. The pass energy for full-spectrum scanning is 100 eV, and the step size is 1 eV; for narrow-spectrum scanning, the pass energy is 30 eV, and the step size is 0.1 eV. Binding energies were calibrated against surface contamination C 1s (284.8 eV). The acquired raw data were processed with *Avantage*, and N 1s (∼402.67 eV) and S $2p_{3/2}$ (∼162.70 eV) orbitals were analyzed as the representatives for the quaternary ammonium group in C5 and total thiols, respectively. The ratios of quaternary ammonium N-to-S were calculated and used to determine the percentages of C5 and MUA ligands capped on the GNC surface.

TEM Sample Preparation. The TEM samples of all GNCs were prepared by diluting the stock solution with ultrapure water (18.2 MΩ, Milli-Q Advantage A10, Millipore) to a final concentration of ∼0.1 μg mL^{-1}, and then a 10 μL sample was deposited onto the ultrathin copper mesh. The copper mesh was dried and observed using a Titan Themis G2 double spherical aberration-corrected transmission electron microscope in HADDF-STEM mode.

For tissue sampling, freshly dissected LNs were fixed in 2.5% glutaraldehyde overnight at 4 °C. The sample was rinsed twice with PBS for 15 min each time and then gradiently dehydrated with ethanol solution (including 30%, 50%, 70%, 80%, 90%, and 95%, every 15 min) and 100% ethanol for 20 min. Acetone was used as a solvent replacement for 20 min. The sample was then incubated with a mixture of embedding agent and acetone (v/v = 1/1) for 1 h, v/v = 3/1 for 3 h, and the pure-embedding agent. After maintaining a constant temperature of 70 °C overnight, the sample was sliced on the LEICA EM UC7 ultrathin microtome to obtain 70−90 nm slices. After drying, the sample was captured with copper mesh and observed on a biological electron microscope (HT7700, HITACHI).

For silver staining, the prepared copper mesh was treated with an AURION R-Gent SE-EM silver staining kit following the instructions. The incubation time was set to ∼25 min to obtain an appropriate contrast signal.

Frozen Section and Immunostaining. The LN tissue was fixed with a 4% paraformaldehyde solution overnight and then washed and soaked in 20% and 30% sucrose solution, respectively, until it sank to the bottom. After that, the sample was removed and frozen in the embedding agent (Tissue-Tek O.C.T. Compound 4583). The frozen slice was made with a Leica CM1950 cryostat, and the section thickness was 5 μm. The sections were placed onto a glass slide coated with 3-aminopropyltriethoxysilane (APES), naturally dried, and stored at 4 °C.

The GNC NIR-II fluorescence within sections was monitored directly using a NIR-II microscopic imaging system with 10× magnification via 808 nm laser excitation. The laser power was adjusted to 50 mW cm^{-2}.

The gold signal was enhanced with silver staining before immunostaining. The glass slides were treated with an AURION R-Gent SE-LM silver staining kit following the instructions. The incubation time was controlled at ∼35 min under room temperature. The silver staining can be observed with a normal upright biological microscope (DM750, Leica, equipped with an ICC50W camera).

The sections were rinsed with Tris-HCl buffer saline + Tween 20 (TBST) thrice before immunofluorescence staining. The samples were incubated in a 10% goat serum solution for antigen blocking. After removing excess liquid, the primary antibodies were added, and the sections were incubated overnight at 4 °C and rinsed with TBST, followed by the addition of secondary antibodies. After a 1 h incubation at room temperature, the sections were rinsed and incubated with a ready-to-use 4′,6-diamidino-2-phenylindole (DAPI) staining solution for 5 min and rinsed again. The sample was mounted with the antiquenching agent and was observed using a Nikon A1R laser scanning confocal microscope. The SCS macrophage cells were stained using rabbit anti-CD169 antibody (ab183356, Abcam; 1:200) followed by goat antirabbit IgG H+L (Alexa Fluor 647) (ab150079, Abcam; 1:400). The germinal center was stained with purified rat anti-GL7 antibody (144602, Biolegend; 1:300), followed by goat antirat IgG H+L (Alexa Fluor 555) (ab150158, Abcam; 1:400). For

the terminal deoxynucleotidyl transferase-mediated dUTP-biotin nick end labeling (TUNEL) assay, the positive apoptosis cells were characterized with a TUNEL assay kit (green fluorescence, Servicebio, G1501) and labeled with fluorescein isothiocyanate (FITC) according to the kit instructions.

For the immunohistochemistry assay, the paraffin-embedded sections were sequentially treated in xylene I 15 min−xylene II 15 min−xylene III 15 min−anhydrous ethanol I 5 min−anhydrous ethanol II 5 min−85% alcohol 5 min−75% alcohol 5 min and distilled water to rinse. Then the dewaxed sections were placed in an antigen retrieval box filled with citric acid antigen retrieval buffer, heated for 8 min to boiling, stopped for 8 min, and turned to medium and low heat for 7 min. After natural cooling, the slides were placed in PBS (pH = 7.4) and washed 3 times with shaking on a decolorizing shaker, 5 min each time. The sections were placed in 3% hydrogen peroxide solution, and incubated at room temperature for 25 min, and the slides were placed in PBS and washed 3 times with shaking on a decolorizing shaker to block the endogenous peroxidase. After that, 3% BSA was added dropwise to cover the tissues evenly and sealed at room temperature for 30 min. Then, the blocking solution was gradually removed, and PBS was added with a certain ratio of Anti-Ki67 Rabbit pAb (GB111499, Servicebio; 1:500) to the slices and placed in a humidified box at 4 °C and incubated overnight. The slides were placed in PBS and washed 3 times, 5 min each time. Horseradish peroxidase (HRP) conjugated goat antirabbit IgG (H+L) secondary antibody (GB23303, Servicebio; 1:500) was added to cover the tissue, and the slices were incubated at room temperature for 50 min. The substrate of HRP, 3,3′-diaminobenzidine tetrahydrochloride (DAB), was used for color development, with a positive signal indicating brown color. The slides were placed in PBS and washed 3 times with shaking, 5 min each. A freshly prepared DAB color developing solution (G1211, Servicebio) was added after the sections were slightly dried, and the color development time under the microscope was controlled. The sections were rinsed with distilled water to stop the color development. Subsequently, the slides were counterstained with hematoxylin (G1004, Servicebio) for ∼3 min, rinsed, differentiated for a few seconds with hematoxylin differentiation solution (G1039, Servicebio), rinsed, blued with hematoxylin blue solution (G1040, Servicebio), and rinsed with running water. The slides were immersed in 75% alcohol 5 min—85% alcohol 5 min—anhydrous ethanol I 5 min—anhydrous ethanol II 5 min—n-butanol 5 min, and xylene 5 min for dehydration and transparency. The slices were mounted with neutral balsam.

H&E Staining. The fixed tissue specimen was cut out and put in the embedding box. Then, 70%, 75%, 80%, 95%, and 100% alcohol were used for gradient dehydration, followed by paraffin wax embedding. After embedding, the samples were sectioned with Leica 2235 microtome, with a section thickness of 4 μm. The paraffin sections were dewaxed thrice, 15 min each, and rehydrated with gradient alcohol (from high to low concentration 100%, 95%, 90%, 80%, 70%, every 2 min) and put in hematoxylin dye solution for 5 min, rinsed with running water, and put in 0.5% hydrochloric acid alcohol solution for differentiation for 5 s, rinsed with running water again, and put in 1% eosin dye solution for 3 min. After gradient dehydration again, xylene was added to transparent samples for 20−30 min. The slices were mounted with resin and scanned with a digital pathology scanner (Pannoramic MIDI, 3D HISTECH).

PAS Staining. The paraffin-embedded sections were dewaxed according to the above process and stained with a PAS staining kit (G1008, Servicebio). The sections were immersed in PAS staining solution B for 10−15 min, washed with tap water, and distilled water twice. The sections were immersed in PAS staining solution A for 25−30 min with light-shielding and rinsed with running water for 5 min. Subsequently, the sections were stained with PAS staining solution C for 30 s, washed with tap water, differentiated with HCl solution, washed with water, blued with ammonia solution, and rinsed with running water. Finally, the sections were dehydrated and mounted with neutral resin. After PAS staining, the glycogen and tissues containing polysaccharides are purple-red, and the cell nucleus is light blue.

Masson Staining. The paraffin-embedded sections were dewaxed according to the above process and stained with a Masson staining kit (G1006, Servicebio). The slices were immersed in Masson A solution overnight and washed with tap water. Then, the mixed solution of Masson B and C in equal proportions was added onto sections and soaked for 1 min. The slices were washed with tap water, differentiated with 1% hydrochloric acid and alcohol, and washed again and then immersed in Masson D and E solutions for 6 and 1 min each. The slices were then dipped into Masson F solution for 20−30 s, rinsed and differentiated with 1% glacial acetic acid, and dehydrated in two tanks of absolute ethanol. The slices were placed into the third tank of absolute ethanol for 5 min, made transparent with xylene for 5 min, and mounted with neutral balsam.

***In Vitro* Wound-Healing Assay.** A wound-healing assay was conducted to investigate cell migration and proliferation visually. HUH-7 cells (ATCC PTA-4583) were inoculated 5×10^5 mL^{-1} into a 24-well plate and cultivated for 16 h to almost cover the bottom of the wells. After cell adhesion, a pipet tip was used to make a straight scratch on the cell layer along the ruler, and each well was washed with PBS thrice. PBS and different concentrations of MTX-GNCs were added to each well, and the plate was incubated and removed after a 12-, 24-, or 36-h incubation for gap width measurement and photographing. The images were processed with *ImageJ*.

Cell Viability Test. After treatment with the GNC, the cell viability of HUVECs (ATCC PCS-100-010) was measured using the 3-(4,5-dimethyl-2-thiazolyl)-2,5-diphenyltetrazolium bromide (MTT) method and characterized with cell living and death staining. Specifically, the HUVECs were preincubated 5×10^5 mL^{-1} overnight in a 96-well plate. The GNC was added to each well of the 96-well plate, and the plate was further incubated for 1 day. After that, the working solution containing MTT (5 mg mL^{-1}) was used to replace the original medium. After 4 h, the solution was absorbed by a thick stack of napkins, and purple sediment was dissolved in 150 μL of DMSO. The mixture was pumped several times with a pipet and placed on a shaker for 10 min to dissolve the crystals fully. The absorbance at 570 nm was measured with a microplate reader (Synergy H1, BioTek).

Animal Experiments. All animal experiments were conducted in compliance with the relevant laws and institutional guidelines and the Institutional Animal Care and Use Committee (IACUC) ethical requirements for animal experiments, with animal experiment welfare and ethical approval (No: TOP-IACUC-2021-0063). The mice (BALB/c, female, 6−8 weeks old, ∼18 g) were purchased from Charles River and temporarily housed in a barrier facility in the animal center. Specifically, the temperature was controlled from 20 to 26 °C. The relative humidity was between 40% and 70%. The air flow in the cages was controlled at 0.2 m s^{-1}, and the minimum static pressure difference was 10 Pa. The animals were fed once a day with water renewed. All the images taken were viewed with *PSLViewer*.

***In Vivo* LN Imaging Effect Comparison.** GNCs were administered (100 μL; 1 mg mL^{-1}; ∼ 5 mg kg^{-1}) through the tail vein or hind limb footpad and detected with a NIR-II animal imager (NIROPTICS, Series III 900/1700) equipped with 808 nm laser source. A 1020 nm long-pass filter (same below) was used for bioimaging and surgical operations. The photos of the supine and prone positions were taken separately. The metabolic procedure was checked every 2 days. The urine sample was collected every hour post intravenous administration by placing a group of three mice in each metabolic cage.

After 3 days of administration with 40 mg kg^{-1} the MUA-GNC, the mice were sacrificed for blood routine and liver and kidney function tests. The blood samples were collected with anticoagulant or procoagulant test tubes with serum separating gel for each group. The latter ones were centrifuged at 2500 rpm for 15 min to promote serum separation. The entire blood samples were sent to an animal blood cell analyzer (DF55Vet, DYMIND) for analysis, while the serum samples were sent to a fully automatic bioanalysis machine (MS480, MedicalSystem) for biochemical index analysis.

For the photostability test, the initial ICG concentration was set as ∼200 μM, and the fluorescence brightness of the GNC was adjusted

to be similar to that of ICG (∼32 μg mL^{-1}). The photostability comparison was performed by exposure to an 808 nm laser irradiation (20 mW cm^{-2}) or natural light irradiation.

Pharmacokinetic Test. Mice were randomly divided into six groups and received at injection of ∼20 mg kg^{-1} the MUA-GNC (Au content: 10 mg kg^{-1}) *via* the tail vein. At certain defined time points (e.g., 0.5, 1, 2, 4, 8, and 12 h), the blood samples were collected from mice in each group, accompanied by the sacrifice of individuals for organ collection. The organs were then weighed and ground into tissue homogenates with a tissue grinder (KZ-III-FP, Servicebio). The blood samples (200 μL each) were sent for thorough digestion with freshly prepared aqua regia and boiled together with the tissue homogenates. Aqua regia was continuously added and evaporated until only white ash and salt remained. The samples were then dissolved with 2% nitric acid solution and diluted 10 times to 3 mL and then sent to an ICP-MS (7700X, Agilent) for Au element analysis. Finally, the measured Au contents (taking into account the dilution factor) were divided by the original organ weights to obtain the weighted average Au content values.

Macrophage Inhibition Model Construction. Macrophage inhibition was achieved by dissolving GdCl$_3$ with normal saline to prepare a 4 mg mL^{-1} GdCl$_3$ solution.[72] Three days before the experiment, a 100 μL GdCl$_3$ solution was injected into the hind limb footpad of mice, and PBS was used as the negative control.

Surgical Guiding and Metastatic LN Removal. The tumor-bearing model was constructed by injecting a human hepatic carcinoma cell Hep 3B cell suspension (ATCC HB-8064, 1 × 10^7 mL^{-1}, 100 μL) on the left hind limb footpad subcutaneously or intraperitoneally. The GNC was injected from the ipsilateral footpad after the tumor diameter had reached ∼6 mm, and the LN accumulating effect was monitored for 6 h. The mice were then sacrificed, and abnormal LNs were removed from the body via surgery, guided with a NIR imager (25 ms, 20 mW cm^{-2}).

In Vivo **LN Metastasis Treatment.** Mice were randomly divided into five groups, with five mice in each group. The tumor LN metastatic model was constructed by injecting a Hep3B cell suspension (ATCC HB-8064, 1 × 10^7 mL^{-1}, 100 μL) into the left hind footpad and then incubated for 4 days to construct the LN metastatic model in the ipsilateral popliteal LN of the injection position. Different groups were treated with 100 μL of PBS, MUA-GNC, MTX-GNC, or free MTX. Each dose of free MTX, the MUA-GNC, or the MTX-GNC was 5, 20, 10 (low), or 20 mg kg^{-1} (high), respectively, for these *in vitro* tests. Mice were administered the above dose once every 2 days, and their body weights were tracked. After 12 days, we anesthetized the mice for weighing, collected the blood samples, sacrificed them to collect the main organs, and dissected the ipsilateral popliteal LN on the injection site.

Software Open Access. The code of the self-developed program is Open Access and uploaded onto GitHub (https://github.com/Yangjie-SUSTC/Lympha_segmentation).

ASSOCIATED CONTENT

ⓢ Supporting Information

The Supporting Information is available free of charge at https://pubs.acs.org/doi/10.1021/acsnano.2c03752.

Video to show GNC-based imaging-guided resection of lymph nodes with metastasis (MP4)

Schematic diagrams of the synthetic routes of HS-MTX ligand and triligand Au$_{25}$ GNC; mass spectrum and ^{1}H NMR spectrum of HS-MTX ligand; deconvoluted ESI-MS results of single (C$_5$/MUA/MUP/MUS)- and dual-ligand GNCs; NIR-II fluorescence images of dual-ligand GNCs prepared with increasing feed percentages (0–100%) of MUA/MUP/MUS; stability results of dual-ligand GNCs with different MUA feed percentages (0–100%) in human serum; NIR fluorescence images of urine samples collected at each hour after intravenous administration of dual-ligand GNCs with different MUA feed percentages (0–100%); agarose gel electrophoresis result of GNCs prepared with a 20–80% MUA ligand feed in the absence and presence of human serum; *in vivo* biodistribution fluorescence figures of dual-ligand (MUP-C$_5$/MUS-C$_5$) GNCs after intravenous injection; *in vivo* biodistribution fluorescence figures of dual-ligand (MUP-C$_5$/MUS-C$_5$) GNCs after footpad injection; NIR-II fluorescence imaging properties of MUA-GNC in comparison with ICG; NIR-II fluorescence imaging application of MUA-GNC in heterotopic tumor-bearing mice; pharmacokinetic profile of MUA-GNC in plasma; pharmacokinetics of MUA-GNC within the main organs of mice; metabolic time and biocompatibility analysis of the MUA-GNC post *in vivo* administration; blood biochemical and blood routine indices for biosafety evaluation; comparison of properties of triligand MTX-GNC and unmodified MUA-GNC; images showing the antiproliferation effect of MTX-GNC on the HuH-7 cell line; NIR-II fluorescence image showing binding of MTX-GNC with HUH-7 cells; stability of MTX-GNC in different body fluid simulation environments; nephrotoxicity reduction and antitumor properties of MTX-GNC (PDF)

AUTHOR INFORMATION

Corresponding Authors

Dejian Zhou − *School of Chemistry and Astbury Centre for Structural Molecular Biology, University of Leeds, Leeds LS2 9JT, United Kingdom;* ⓞ orcid.org/0000-0003-3314-9242; Email: d.zhou@leeds.ac.uk

Xingyu Jiang − *Guangdong Provincial Key Laboratory of Advanced Biomaterials and Shenzhen Key Laboratory of Smart Healthcare Engineering, Department of Biomedical Engineering, Southern University of Science and Technology, Shenzhen, Guangdong 518055, P. R. China;* ⓞ orcid.org/0000-0002-5008-4703; Email: jiang@sustech.edu.cn

Authors

Zeyang Pang − *Guangdong Provincial Key Laboratory of Advanced Biomaterials and Shenzhen Key Laboratory of Smart Healthcare Engineering, Department of Biomedical Engineering, Southern University of Science and Technology, Shenzhen, Guangdong 518055, P. R. China; School of Chemistry and Astbury Centre for Structural Molecular Biology, University of Leeds, Leeds LS2 9JT, United Kingdom*

Weixiao Yan − *Guangdong Provincial Key Laboratory of Advanced Biomaterials and Shenzhen Key Laboratory of Smart Healthcare Engineering, Department of Biomedical Engineering, Southern University of Science and Technology, Shenzhen, Guangdong 518055, P. R. China*

Jie Yang − *Guangdong Provincial Key Laboratory of Advanced Biomaterials and Shenzhen Key Laboratory of Smart Healthcare Engineering, Department of Biomedical Engineering, Southern University of Science and Technology, Shenzhen, Guangdong 518055, P. R. China*

Qizhen Li − *Guangdong Provincial Key Laboratory of Advanced Biomaterials and Shenzhen Key Laboratory of Smart Healthcare Engineering, Department of Biomedical Engineering, Southern University of Science and Technology, Shenzhen, Guangdong 518055, P. R. China*

Yuan Guo − *School of Food Science and Nutrition and Astbury Centre for Structural Molecular Biology, University*

of Leeds, Leeds LS2 9JT, United Kingdom; ◉ orcid.org/
0000-0003-4607-7356

Complete contact information is available at:
https://pubs.acs.org/10.1021/acsnano.2c03752

Author Contributions

X.J. and D.Z. conceived the idea and provided guidance and financial support for the project. Z.P. designed and performed all the experiments and data analyses except those stated below. W.Y. performed all the animal experiments and obtained the near-infrared images. J.Y. wrote the software for the automatic recognition of the mouse body outline and lower-body lymph nodes. Q.L. and Y.G. performed TEM imaging. Z.P. wrote the manuscript with input from all authors.

Notes

The authors declare no competing financial interest.

REFERENCES

(1) Lee, W. C.; Kopetz, S.; Wistuba, I. I.; Zhang, J. Metastasis of Cancer: When and How? Ann. Oncol. 2017, 28 (9), 2045−2047.

(2) Wang, J.; Lu, W.; Tang, C.; Liu, Y.; Sun, J.; Mu, X.; Zhang, L.; Dai, B.; Li, X.; Zhuo, H.; Jiang, X. Label-Free Isolation and MRNA Detection of Circulating Tumor Cells from Patients with Metastatic Lung Cancer for Disease Diagnosis and Monitoring Therapeutic Efficacy. Anal. Chem. 2015, 87 (23), 11893−11900.

(3) Hu, X. X.; He, P. P.; Qi, G. B.; Gao, Y. J.; Lin, Y. X.; Yang, C.; Yang, P. P.; Hao, H.; Wang, L.; Wang, H. Transformable Nanomaterials as an Artificial Extracellular Matrix for Inhibiting Tumor Invasion and Metastasis. ACS Nano 2017, 11 (4), 4086−4096.

(4) Chaffer, C. L.; Weinberg, R. A. A Perspective on Cancer Cell Metastasis. Science 2011, 331 (6024), 1559−1564.

(5) Heerdt, A. S. Lymphatic Mapping and Sentinel Lymph Node Biopsy for Breast Cancer. JAMA Oncol. 2018, 4 (3), 431.

(6) Sestito, L. F.; Thomas, S. N. Biomaterials for Modulating Lymphatic Function in Immunoengineering. ACS Pharmacol. Transl. Sci. 2019, 2 (5), 293−310.

(7) Zhang, X.-Y.; Lu, W.-Y. Recent Advances in Lymphatic Targeted Drug Delivery System for Tumor Metastasis. Cancer Biol. Med. 2014, 11 (4), 247−254.

(8) Torous, V. F.; Oliva, E. On the New (Version 9) American Joint Committee on Cancer Tumor, Node, Metastasis Staging for Cervical Cancer—A Commentary. Cancer Cytopathol. 2021, 129 (8), 581−582.

(9) Li, C.; Torres, V. C.; Tichauer, K. M. Noninvasive Detection of Cancer Spread to Lymph Nodes: A Review of Molecular Imaging Principles and Protocols. J. Surg. Oncol. 2018, 118 (2), 301−314.

(10) Sun, Y.; Ding, M.; Zeng, X.; Xiao, Y.; Wu, H.; Zhou, H.; Ding, B.; Qu, C.; Hou, W.; Er-bu, A. G. A.; Zhang, Y.; Cheng, Z.; Hong, X. Novel Bright-Emission Small-Molecule NIR-II Fluorophores for in Vivo Tumor Imaging and Image-Guided Surgery. Chem. Sci. 2017, 8 (5), 3489−3493.

(11) Lin, H.; Zhou, Y.; Wang, J.; Wang, H.; Yao, T.; Chen, H.; Zheng, H.; Zhang, Y.; Ren, E.; Jiang, L.; Chu, C.; Chen, X.; Mao, J.; Wang, F.; Liu, G. Repurposing ICG Enables MR/PA Imaging Signal Amplification and Iron Depletion for Iron-Overload Disorders. Sci. Adv. 2021, 7 (51), No. eabl5862.

(12) He, P. S.; Li, F.; Li, G. H.; Guo, C.; Chen, T. J. The Combination of Blue Dye and Radioisotope versus Radioisotope Alone during Sentinel Lymph Node Biopsy for Breast Cancer: A Systematic Review. BMC Cancer 2016, 16 (1), 107 DOI: 10.1186/s12885-016-2137-0.

(13) Bennett, Z. T.; Feng, Q.; Bishop, J. A.; Huang, G.; Sumer, B. D.; Gao, J. Detection of Lymph Node Metastases by Ultra-PH-Sensitive Polymeric Nanoparticles. Theranostics 2020, 10 (7), 3340−3350.

(14) Qiu, S.; Zeng, J.; Hou, Y.; Chen, L.; Ge, J.; Wen, L.; Liu, C.; Zhang, Y.; Zhu, R.; Gao, M. Detection of Lymph Node Metastasis with Near-Infrared Upconversion Luminescent Nanoprobes. Nanoscale 2018, 10 (46), 21772−21781.

(15) Zhang, X. D.; Chen, J.; Luo, Z.; Wu, D.; Shen, X.; Song, S. S.; Sun, Y. M.; Liu, P. X.; Zhao, J.; Huo, S.; Fan, S.; Fan, F.; Liang, X. J.; Xie, J. Enhanced Tumor Accumulation of Sub-2 Nm Gold Nanoclusters for Cancer Radiation Therapy. Adv. Healthc. Mater. 2014, 3 (1), 133−141.

(16) Almeida, J. P. M.; Lin, A. Y.; Figueroa, E. R.; Foster, A. E.; Drezek, R. A. In Vivo Gold Nanoparticle Delivery of Peptide Vaccine Induces Anti-Tumor Immune Response in Prophylactic and Therapeutic Tumor Models. Small 2015, 11 (12), 1453−1459.

(17) Dykman, L. A.; Khlebtsov, N. G. Immunological Properties of Gold Nanoparticles. Chem. Sci. 2017, 8 (3), 1719−1735.

(18) Yang, X.; Yang, J.; Wang, L.; Ran, B.; Jia, Y.; Zhang, L.; Yang, G.; Shao, H.; Jiang, X. Pharmaceutical Intermediate-Modified Gold Nanoparticles: Against Multidrug-Resistant Bacteria and Wound-Healing Application via an Electrospun Scaffold. ACS Nano 2017, 11 (6), 5737−5745.

(19) Wang, L.; Yang, J.; Li, S.; Li, Q.; Liu, S.; Zheng, W.; Jiang, X. Oral Administration of Starting Materials for In Vivo Synthesis of Antibacterial Gold Nanoparticles for Curing Remote Infections. Nano Lett. 2021, 21 (2), 1124−1131.

(20) Pang, Z.; Li, Q.; Jia, Y.; Yan, W.; Qi, J.; Guo, Y.; Hu, F.; Zhou, D.; Jiang, X. Controlling the Pyridinium-Zwitterionic Ligand Ratio on Atomically Precise Gold Nanoclusters Allowing for Eradicating Gram-Positive Drug-Resistant Bacteria and Retaining Biocompatibility. Chem. Sci. 2021, 12 (44), 14871−14882.

(21) Wang, L.; Hou, Q.; Zheng, W.; Jiang, X. Fluorescent and Antibacterial Aminobenzeneboronic Acid (ABA)-Modified Gold Nanoclusters for Self-Monitoring Residual Dosage and Smart Wound Care. ACS Nano 2021, 15 (11), 17885−17894.

(22) Xie, Y.; Liu, Y.; Yang, J.; Liu, Y.; Hu, F.; Zhu, K.; Jiang, X. Gold Nanoclusters for Targeting Methicillin-Resistant Staphylococcus Aureus In Vivo. Angew. Chem., Int. Ed. 2018, 57 (15), 3958−3962.

(23) Kong, Y.; Chen, J.; Fang, H.; Heath, G.; Wo, Y.; Wang, W.; Li, Y.; Guo, Y.; Evans, S. D.; Chen, S.; Zhou, D. Highly Fluorescent Ribonuclease-A-Encapsulated Lead Sulfide Quantum Dots for Ultrasensitive Fluorescence in Vivo Imaging in the Second Near-Infrared Window. Chem. Mater. 2016, 28 (9), 3041−3050.

(24) Tao, Y.; Ju, E.; Li, Z.; Ren, J.; Qu, X. Engineered CpG-Antigen Conjugates Protected Gold Nanoclusters as Smart Self-Vaccines for Enhanced Immune Response and Cell Imaging. Adv. Funct. Mater. 2014, 24 (7), 1004−1010.

(25) Li, H.; Li, H.; Wan, A. Luminescent Gold Nanoclusters for in Vivo Tumor Imaging. Analyst 2020, 145 (2), 348−363.

(26) Liu, H.; Hong, G.; Luo, Z.; Chen, J.; Chang, J.; Gong, M.; He, H.; Yang, J.; Yuan, X.; Li, L.; Mu, X.; Wang, J.; Mi, W.; Luo, J.; Xie, J.; Zhang, X. Atomic-Precision Gold Clusters for NIR-II Imaging. *Adv. Mater.* **2019**, *31* (46), 1901015.

(27) Kong, Y.; Santos-Carballal, D.; Martin, D.; Sergeeva, N. N.; Wang, W.; Liu, G.; Johnson, B.; Bhayana, B.; Lin, Z.; Wang, Y.; Le Guével, X.; de Leeuw, N. H.; Zhou, D.; Wu, M. X. A NIR-II-Emitting Gold Nanocluster-Based Drug Delivery System for Smartphone-Triggered Photodynamic Theranostics with Rapid Body Clearance. *Mater. Today* **2021**, *51*, 96−107.

(28) Li, D.; Liu, Q.; Qi, Q.; Shi, H.; Hsu, E. C.; Chen, W.; Yuan, W.; Wu, Y.; Lin, S.; Zeng, Y.; Xiao, Z.; Xu, L.; Zhang, Y.; Stoyanova, T.; Jia, W.; Cheng, Z. Gold Nanoclusters for NIR-II Fluorescence Imaging of Bones. *Small* **2020**, *16* (43), 1−9.

(29) Wang, W.; Kong, Y.; Jiang, J.; Xie, Q.; Huang, Y.; Li, G.; Wu, D.; Zheng, H.; Gao, M.; Xu, S.; Pan, Y.; Li, W.; Ma, R.; Wu, M. X.; Li, X.; Zuilhof, H.; Cai, X.; Li, R. Engineering the Protein Corona Structure on Gold Nanoclusters Enables Red-Shifted Emissions in the Second Near-Infrared Window for Gastrointestinal Imaging. *Angew. Chem., Int. Ed.* **2020**, *59* (50), 22431−22435.

(30) Song, X.; Zhu, W.; Ge, X.; Li, R.; Li, S.; Chen, X.; Song, J.; Xie, J.; Chen, X.; Yang, H. A New Class of NIR-II Gold Nanocluster-Based Protein Biolabels for In Vivo Tumor-Targeted Imaging. *Angew. Chem., Int. Ed.* **2021**, *60* (3), 1306−1312.

(31) Yu, Z.; Musnier, B.; Wegner, K. D.; Henry, M.; Chovelon, B.; Desroches-Castan, A.; Fertin, A.; Resch-Genger, U.; Bailly, S.; Coll, J. L.; Usson, Y.; Josserand, V.; Le Guével, X. High-Resolution Shortwave Infrared Imaging of Vascular Disorders Using Gold Nanoclusters. *ACS Nano* **2020**, *14* (4), 4973−4981.

(32) Tang, L.; Zeng, X.; Zhou, H.; Gui, C.; Luo, Q.; Zhou, W.; Wu, J.; Li, Q.; Li, Y.; Xiao, Y. Theranostic Gold Nanoclusters for NIR-II Imaging and Photodynamic Therapy. *Chem. Res. Chinese Univ.* **2021**, *37* (4), 934−942.

(33) Trevaskis, N. L.; Kaminskas, L. M.; Porter, C. J. H. From Sewer to Saviour-Targeting the Lymphatic System to Promote Drug Exposure and Activity. *Nat. Rev. Drug Discovery* **2015**, *14* (11), 781−803.

(34) Nishimoto, Y.; Nagashima, S.; Nakajima, K.; Ohira, T.; Sato, T.; Izawa, T.; Yamate, J.; Higashikawa, K.; Kuge, Y.; Ogawa, M.; Kojima, C. Carboxyl-, Sulfonyl-, and Phosphate-Terminal Dendrimers as a Nanoplatform with Lymph Node Targeting. *Int. J. Pharm.* **2020**, *576*, 119021.

(35) Ye, T.; Zhang, W.; Sun, M.; Yang, R.; Song, S.; Mao, Y.; Yao, J.; Yang, X.; Wang, S.; Pan, W. Study on Intralymphatic-Targeted Hyaluronic Acid-Modified Nanoliposome: Influence of Formulation Factors on the Lymphatic Targeting. *Int. J. Pharm.* **2014**, *471* (1−2), 245−257.

(36) Murthy, A. K.; Stover, R. J.; Hardin, W. G.; Schramm, R.; Nie, G. D.; Gourisankar, S.; Truskett, T. M.; Sokolov, K. V.; Johnston, K. P. Charged Gold Nanoparticles with Essentially Zero Serum Protein Adsorption in Undiluted Fetal Bovine Serum. *J. Am. Chem. Soc.* **2013**, *135* (21), 7799−7802.

(37) Schudel, A.; Francis, D. M.; Thomas, S. N. Material Design for Lymph Node Drug Delivery. *Nat. Rev. Mater.* **2019**, *4* (6), 415−428.

(38) Jiang, H.; Wang, Q.; Sun, X. Lymph Node Targeting Strategies to Improve Vaccination Efficacy. *J. Controlled Release* **2017**, *267* (July), 47−56.

(39) Li, B.; Li, B.; Yuan, Z.; He, Y.; He, Y.; Hung, H. C.; Jiang, S.; Jiang, S. Zwitterionic Nanoconjugate Enables Safe and Efficient Lymphatic Drug Delivery. *Nano Lett.* **2020**, *20* (6), 4693−4699.

(40) Jiang, S.; Cao, Z. Ultralow-Fouling, Functionalizable, and Hydrolyzable Zwitterionic Materials and Their Derivatives for Biological Applications. *Adv. Mater.* **2010**, *22* (9), 920−932.

(41) Khan, Z. A.; Tripathi, R.; Mishra, B. Methotrexate: A Detailed Review on Drug Delivery and Clinical Aspects. *Expert Opin. Drug Delivery* **2012**, *9* (2), 151−169.

(42) Chen, T.; Fung, V.; Yao, Q.; Luo, Z.; Jiang, D. E.; Xie, J. Synthesis of Water-Soluble [Au25(SR)18]- Using a Stoichiometric Amount of NaBH4. *J. Am. Chem. Soc.* **2018**, *140* (36), 11370−11377.

(43) Luo, Z.; Nachammai, V.; Zhang, B.; Yan, N.; Leong, D. T.; Jiang, D. E.; Xie, J. Toward Understanding the Growth Mechanism: Tracing All Stable Intermediate Species from Reduction of Au(I)-Thiolate Complexes to Evolution of Au25nanoclusters. *J. Am. Chem. Soc.* **2014**, *136* (30), 10577−10580.

(44) Aldeek, F.; Muhammed, M. A. H.; Palui, G.; Zhan, N.; Mattoussi, H. Growth of Highly Fluorescent Polyethylene Glycol- and Zwitterion-Functionalized Gold Nanoclusters. *ACS Nano* **2013**, *7* (3), 2509−2521.

(45) Pei, P.; Shen, W.; Zhou, H.; Sun, Y.; Zhong, J.; Liu, T.; Yang, K. Radionuclide Labeled Gold Nanoclusters Boost Effective Anti-Tumor Immunity for Augmented Radio-Immunotherapy of Cancer. *Nano Today* **2021**, *38*, 101144.

(46) Wang, W.; Guo, Y.; Tiede, C.; Chen, S.; Kopytynski, M.; Kong, Y.; Kulak, A.; Tomlinson, D.; Chen, R.; McPherson, M.; Zhou, D. Ultraefficient Cap-Exchange Protocol To Compact Biofunctional Quantum Dots for Sensitive Ratiometric Biosensing and Cell Imaging. *ACS Appl. Mater. Interfaces* **2017**, *9* (18), 15232−15244.

(47) Guo, Y.; Sakonsinsiri, C.; Nehlmeier, I.; Fascione, M. A.; Zhang, H.; Wang, W.; Pöhlmann, S.; Turnbull, W. B.; Zhou, D. Compact, Polyvalent Mannose Quantum Dots as Sensitive, Ratiometric FRET Probes for Multivalent Protein-Ligand Inter-actions. *Angew. Chem., Int. Ed.* **2016**, *55* (15), 4738−4742.

(48) Soo Choi, H.; Liu, W.; Misra, P.; Tanaka, E.; Zimmer, J. P.; Itty Ipe, B.; Bawendi, M. G.; Frangioni, J. V. Renal Clearance of Nanoparticles. *Nat. Biotechnol.* **2007**, *25* (10), 1165−1170.

(49) Yu, M.; Xu, J.; Zheng, J. Renal Clearable Luminescent Gold Nanoparticles: From the Bench to the Clinic. *Angew. Chem.* **2019**, *131* (13), 4156−4172.

(50) Cheng, Q.; Wei, T.; Farbiak, L.; Johnson, L. T.; Dilliard, S. A.; Siegwart, D. J. Selective Organ Targeting (SORT) Nanoparticles for Tissue-Specific MRNA Delivery and CRISPR-Cas Gene Editing. *Nat. Nanotechnol.* **2020**, *15* (4), 313−320.

(51) Nakamura, T.; Kawai, M.; Sato, Y.; Maeki, M.; Tokeshi, M.; Harashima, H. The Effect of Size and Charge of Lipid Nanoparticles Prepared by Microfluidic Mixing on Their Lymph Node Transitivity and Distribution. *Mol. Pharmaceutics* **2020**, *17* (3), 944−953.

(52) Du, B.; Jiang, X.; Das, A.; Zhou, Q.; Yu, M.; Jin, R.; Zheng, J. Glomerular Barrier Behaves as an Atomically Precise Bandpass Filter in a Sub-Nanometre Regime. *Nat. Nanotechnol.* **2017**, *12* (11), 1096−1102.

(53) Porret, E.; Le Guével, X.; Coll, J. L. Gold Nanoclusters for Biomedical Applications: Toward: In Vivo Studies. *J. Mater. Chem. B* **2020**, *8* (11), 2216−2232.

(54) Nakajima, Y.; Asano, K.; Mukai, K.; Urai, T.; Okuwa, M.; Sugama, J.; Nakatani, T. Near-Infrared Fluorescence Imaging Directly Visualizes Lymphatic Drainage Pathways and Connections between Superficial and Deep Lymphatic Systems in the Mouse Hindlimb. *Sci. Rep.* **2018**, *8*, 7078 DOI: 10.1038/s41598-018-25383-y.

(55) Van den Broeck, W.; Van den; Derore, A.; Simoens, P. Anatomy and Nomenclature of Murine Lymph Nodes: Descriptive Study and Nomenclatory Standardization in BALB/CAnNCrl Mice. *J. Immunol. Methods* **2006**, *312* (1−2), 12−19.

(56) Kobayashi, H.; Kawamoto, S.; Star, R. A.; Waldmann, T. A.; Tagaya, Y.; Brechbiel, M. W. Micro-Magnetic Resonance Lymphan-giography in Mice Using a Novel Dendrimer-Based Magnetic Resonance Imaging Contrast Agent. *Cancer Res.* **2003**, *63* (2), 271−276.

(57) Tian, R.; Ma, H.; Zhu, S.; Lau, J.; Ma, R.; Liu, Y.; Lin, L.; Chandra, S.; Wang, S.; Zhu, X.; Deng, H.; Niu, G.; Zhang, M.; Antaris, A. L.; Hettie, K. S.; Yang, B.; Liang, Y.; Chen, X. Multiplexed NIR-II Probes for Lymph Node-Invaded Cancer Detection and Imaging-Guided Surgery. *Adv. Mater.* **2020**, *32* (11), 1907365.

(58) Antaris, A. L.; Chen, H.; Diao, S.; Ma, Z.; Zhang, Z.; Zhu, S.; Wang, J.; Lozano, A. X.; Fan, Q.; Chew, L.; Zhu, M.; Cheng, K.; Hong, X.; Dai, H.; Cheng, Z. A High Quantum Yield Molecule-Protein Complex Fluorophore for near-Infrared II Imaging. *Nat. Commun.* **2017**, *8*, 15269 DOI: 10.1038/ncomms15269.

(59) Le Guével, X.; Henry, M.; Motto-Ros, V.; Longo, E.; Montañez, M. I.; Pelascini, F.; De La Rochefoucauld, O.; Zeitoun, P.; Coll, J. L.; Josserand, V.; Sancey, L. Elemental and Optical Imaging Evaluation of Zwitterionic Gold Nanoclusters in Glioblastoma Mouse Models. *Nanoscale* **2018**, *10* (39), 18657−18664.

(60) Fiurasek, P.; Reven, L. Phosphonic and Sulfonic Acid-Functionalized Gold Nanoparticles: A Solid-State NMR Study. *Langmuir* **2007**, *23* (5), 2857−2866.

(61) Balachandran, Y. L.; Li, X.; Jiang, X. Integrated Microfluidic Synthesis of Aptamer Functionalized Biozeolitic Imidazolate Framework (BioZIF-8) Targeting Lymph Node and Tumor. *Nano Lett.* **2021**, *21* (3), 1335−1344.

(62) Yáñez, J. A.; Wang, S. W. J.; Knemeyer, I. W.; Wirth, M. A.; Alton, K. B. Intestinal Lymphatic Transport for Drug Delivery. *Adv. Drug Delivery Rev.* **2011**, *63* (10−11), 923−942.

(63) Zhu, S.; Yung, B. C.; Chandra, S.; Niu, G.; Antaris, A. L.; Chen, X. Near-Infrared-II (NIR-II) Bioimaging via Off-Peak NIR-I Fluorescence Emission. *Theranostics* **2018**, *8* (15), 4141−4151.

(64) Porcu, E. P.; Salis, A.; Gavini, E.; Rassu, G.; Maestri, M.; Giunchedi, P. Indocyanine Green Delivery Systems for Tumour Detection and Treatments. *Biotechnol. Adv.* **2016**, *34* (5), 768−789.

(65) Peng, X.; Wang, J.; Zhou, F.; Liu, Q.; Zhang, Z. Nanoparticle-Based Approaches to Target the Lymphatic System for Antitumor Treatment. *Cell. Mol. Life Sci.* **2021**, *78* (12), 5139−5161.

(66) Mok, H.; Jeong, H.; Kim, S. J.; Hyun Chung, B. Indocyanine Green Encapsulated Nanogels for Hyaluronidase Activatable and Selective near Infrared Imaging of Tumors and Lymph Nodes. *Chem. Commun.* **2012**, *48* (69), 8628−8630.

(67) Alander, J. T.; Kaartinen, I.; Laakso, A.; Pätilä, T.; Spillmann, T.; Tuchin, V. V.; Venermo, M.; Välisuo, P. A Review of Indocyanine Green Fluorescent Imaging in Surgery. *Int. J. Biomed. Imaging* **2012**, *2012*, 940585.

(68) Tsujino, Y.; Mizumoto, K.; Matsuzaka, Y.; Niihara, H.; Morita, E. Fluorescence Navigation with Indocyanine Green for Detecting Sentinel Nodes in Extramammary Paget's Disease and Squamous Cell Carcinoma. *J. Dermatol.* **2009**, *36* (2), 90−94.

(69) Egloff-Juras, C.; Bezdetnaya, L.; Dolivet, G.; Lassalle, H. P. NIR Fluorescence-Guided Tumor Surgery: New Strategies for the Use of Indocyanine Green. *Int. J. Nanomedicine* **2019**, *14*, 7823−7838.

(70) Louie, D. A. P.; Liao, S. Lymph Node Subcapsular Sinus Macrophages as the Frontline of Lymphatic Immune Defense. *Front. Immunol.* **2019**, *10* (FEB), 1−9.

(71) Schudel, A.; Chapman, A. P.; Yau, M.-K.; Higginson, C. J.; Francis, D. M.; Manspeaker, M. P.; Avecilla, A. R. C.; Rohner, N. A.; Finn, M. G.; Thomas, S. N. Programmable Multistage Drug Delivery to Lymph Nodes. *Nat. Nanotechnol.* **2020**, *15* (6), 491−499.

(72) Zhang, Y.-N.; Poon, W.; Sefton, E.; Chan, W. C. W. Suppressing Subcapsular Sinus Macrophages Enhances Transport of Nanovaccines to Lymph Node Follicles for Robust Humoral Immunity. *ACS Nano* **2020**, *14* (8), 9478−9490.

(73) Cai, T.; Liu, H.; Zhang, S.; Hu, J.; Zhang, L. Delivery of Nanovaccine towards Lymphoid Organs: Recent Strategies in Enhancing Cancer Immunotherapy. *J. Nanobiotechnology* **2021**, *19* (1), 1−23.

(74) Zhang, X. D.; Wu, D.; Shen, X.; Liu, P. X.; Fan, F. Y.; Fan, S. J. In Vivo Renal Clearance, Biodistribution, Toxicity of Gold Nanoclusters. *Biomaterials* **2012**, *33* (18), 4628−4638.

(75) Abolmaali, S. S.; Tamaddon, A. M.; Dinarvand, R. A Review of Therapeutic Challenges and Achievements of Methotrexate Delivery Systems for Treatment of Cancer and Rheumatoid Arthritis. *Cancer Chemother. Pharmacol.* **2013**, *71* (5), 1115−1130.

(76) Maksimovic, V.; Pavlovic-Popovic, Z.; Vukmirovic, S.; Cvejic, J.; Mooranian, A.; Al-Salami, H.; Mikov, M.; Golocorbin-Kon, S. Molecular Mechanism of Action and Pharmacokinetic Properties of Methotrexate. *Mol. Biol. Rep.* **2020**, *47* (6), 4699−4708.

(77) Mioduszewska, K.; Dołżonek, J.; Wyrzykowski, D.; Kubik, Ł.; Wiczling, P.; Sikorska, C.; Toński, M.; Kaczyński, Z.; Stepnowski, P.; Białk-Bielińska, A. Overview of Experimental and Computational Methods for the Determination of the PKa Values of 5-Fluorouracil, Cyclophosphamide, Ifosfamide, Imatinib and Methotrexate. *TrAC - Trends Anal. Chem.* **2017**, *97*, 283−296.

(78) Meloun, M.; Ferenčíková, Z.; Kaštánek, M.; Vrána, A. Thermodynamic Dissociation Constants of Butorphanol and Zolpidem by the Least-Squares Nonlinear Regression of Multiwavelength Spectrophotometric PH-Titration Data. *J. Chem. Eng. Data* **2011**, *56*, 1009−1019.

(79) Chen, Y.-H.; Tsai, C.-Y.; Huang, P.-Y.; Chang, M.-Y.; Cheng, P.-C.; Chou, C.-H.; Chen, D.-H.; Wang, C.-R.; Shiau, A.-L.; Wu, C.-L. Methotrexate Conjugated to Gold Nanoparticles Inhibits Tumor Growth in a Syngeneic Lung Tumor Model. *Mol. Pharmaceutics* **2007**, *4* (5), 713−722.

(80) Budhadev, D.; Poole, E.; Nehlmeier, I.; Liu, Y.; Hooper, J.; Kalverda, E.; Akshath, U. S.; Hondow, N.; Turnbull, W. B.; Pöhlmann, S.; Guo, Y.; Zhou, D. Glycan-Gold Nanoparticles as Multifunctional Probes for Multivalent Lectin-Carbohydrate Binding: Implications for Blocking Virus Infection and Nanoparticle Assembly. *J. Am. Chem. Soc.* **2020**, *142* (42), 18022−18034.

(81) Uchihara, Y.; Komori, R.; Tago, K.; Tamura, H.; Funakoshi-Tago, M. Methotrexate Significantly Induces Apoptosis by Inhibiting STAT3 Activation in NPM-ALK-Positive ALCL Cells. *Biochem. Pharmacol.* **2019**, *170*, 113666.

(82) Niemelä, E.; Desai, D.; Niemi, R.; Doroszko, M.; Özliseli, E.; Kemppainen, K.; Rahman, N. A.; Sahlgren, C.; Törnquist, K.; Eriksson, J. E.; Rosenholm, J. M. Nanoparticles Carrying Fingolimod and Methotrexate Enables Targeted Induction of Apoptosis and Immobilization of Invasive Thyroid Cancer. *Eur. J. Pharm. Biopharm.* **2020**, *148*, 1−9.

(83) Nyblom, H.; Björnsson, E.; Simrén, M.; Aldenborg, F.; Almer, S.; Olsson, R. The AST/ALT Ratio as an Indicator of Cirrhosis in Patients with PBC. *Liver Int.* **2006**, *26* (7), 840−845.

(84) Ettel, M.; Gonzalez, G. A.; Gera, S.; Eze, O.; Sigal, S.; Park, J. S.; Xu, R. Frequency and Pathological Characteristics of Drug-Induced Liver Injury in a Tertiary Medical Center. *Hum. Pathol.* **2017**, *68*, 92−98.

(85) Matté, C.; Stefanello, F. M.; Mackedanz, V.; Pederzolli, C. D.; Lamers, M. L.; Dutra-Filho, C. S.; dos Santos, M. F.; Wyse, A. T. S. Homocysteine Induces Oxidative Stress, Inflammatory Infiltration, Fibrosis and Reduces Glycogen/Glycoprotein Content in Liver of Rats. *Int. J. Dev. Neurosci.* **2009**, *27* (4), 337−344.

(86) Wang, X. L.; Zhang, T.; Hu, L. H.; Sun, S. Q.; Zhang, W. F.; Sun, Z.; Shen, L. H.; He, B. Comparison of Effects of Different Statins on Contrast-Induced Acute Kidney Injury in Rats: Histopathological and Biochemical Findings. *Oxid. Med. Cell. Longev.* **2017**, *2017*, 6282486.

(87) Cikler-Dulger, E.; Sogut, I. Investigation of the Protective Effects of Boric Acid on Ethanol Induced Kidney Injury. *Biotechnol. Histochem.* **2020**, *95* (3), 186−193.

(88) Stallons, L. J.; Whitaker, R. M.; Schnellmann, R. G. Suppressed Mitochondrial Biogenesis in Folic Acid-Induced Acute Kidney Injury and Early Fibrosis. *Toxicol. Lett.* **2014**, *224* (3), 326−332.

(89) Matulionyte, M.; Dapkute, D.; Budenaite, L.; Jarockyte, G.; Rotomskis, R. Photoluminescent Gold Nanoclusters in Cancer Cells: Cellular Uptake, Toxicity, and Generation of Reactive Oxygen Species. *Int. J. Mol. Sci.* **2017**, *18* (2), 378.